INTERNATIONAL ATOMIC ENERGY AGENCY

FIFTEENTH INTERNATIONAL CONFERENCE ON PLASMA PHYSICS AND CONTROLLED NUCLEAR FUSION RESEARCH

Seville, Spain, 26 September – 1 October 1994 CONF-940933--30

IAEA-CN-60/D-2-II-6

Dynamics of the L → H Transition, VH-Mode Evolution, Edge Localized Modes and R.F. Driven Confinement Control in Tokamaks

P.H. Diamond, V.B. Lebedev, Y.M. Liang, A.V. Gruzinov, I. Gruzinova, M. Medvedev

University of California, San Diego, La Jolla, CA 92093-0319

B.A. Carreras, D.E. Newman, L. Charlton, K.L. Sidikman, D.B. Batchelor, E.F. Jaeger, C.Y. Wang

Fusion Energy Division, Oak Ridge National Laboratory, Oak Ridge, TN 37830

G.G. Craddock, N. Mattor

Lawrence Livermore National Laboratory, Livermore, CA 94551

T.S. Hahm, M. Ono, B. Leblanc and H. Biglari

Princeton Plasma Physics Laboratory, Princeton, NJ 08543

F.Y. Gang and D.J. Sigmar

Plasma Fusion Center, Massachusetts Institute of Technology, Cambridge, MA 02139

DISCLAIMER

Dynamics of the L → H Transition, VH-Mode Evolution, Edge Localized Modes and R.F. Driven Confinement Control in Tokamaks

Abstract

Several novel theoretical results related to L→H transition physics, VH-mode evolution, Edge Localized Modes and active confinement control are presented. Critical issues are identified, results are discussed and important unresolved questions are listed. The basic physics is discussed in the contexts of current experiments and of ITER.

I.) Introduction

The L→H transition[1] is crucial to ITER[2]. Specifically, the confinement enhancement of the H-mode is necessary for an adequate ignition margin, and ELMs are required for efficient ash removal. At the same time, giant ELM Dα-bursts severely challenge divertor technology. The recently discovered VH-mode[3] offers even greater benefits in confinement enhancement but also presents more formidable challenges vis-a-vis termination due to a (likely) kink-induced "monster" ELM. Hence, both a sound scientific understanding of H-mode physics and the ability to actively control[4,5] confinement regime transitions are necessary.

In this paper, we summarize recent advances in L→H transition physics. The body of the paper is organized into four sections which are:

a.) (Section II) Basic L→H Transition Mechanism Physics,
b.) (Section III) VH-Mode Evolution,
c.) (Section IV) Edge Localized Mode (ELM) Dynamics,
d.) (Section V) Active Control of Confinement via RF.

In each section, a statement of the fundamental issues is followed by a summary of the basic model and results obtained from it. Outstanding technical questions are identified and a description of planned future work is provided. A discussion of the broader unresolved issues in this work for L→H transition physics appears in Section VI.

II.) Basic L→H Transition Mechanism

Virtually all credible models of the L→H transition utilize the paradigm of electric field shear-induced suppression of turbulence to explain the formation of a transport barrier[6-9]. Moreover, this theoretical paradigm is strongly supported by experimental findings[10]. Hence, the central issue of the L→H transition mechanism is the origin of the electric field shear layer. Specific questions include:

a.) What are the relative contributions of poloidal velocity shear $\left(V_\theta{}'\right)$ and diamagnetic velocity $\left(V_d{}'\right)$ shear to $V_E{}' = -cE_r{}'/B$?

b.) How do $V_\theta{}'$ and $V_d{}'$ evolve in time at and above the L→H transition threshold?

c.) What is the "seed" which triggers the transition?

d.) What physics determines the L→H power threshold and the empirically determined scalings?

To answer these questions, a simple dynamical model for fluctuation intensity $\left(\overline{E}\right)$ poloidal velocity shear (U) and pressure gradient (N) evolution has been derived from fundamental theoretical principles[11,12]. The model equations are:

$$\frac{\partial \overline{E}}{\partial \tau} = \overline{E}N - \overline{E}^2 - V^2\overline{E}, \tag{1}$$

$$\frac{\partial U}{\partial \tau} = a\overline{E}V - bU, \tag{2}$$

$$\frac{\partial N}{\partial \tau} = -A\overline{E}N - BN + \overline{Q}, \tag{3}$$

$$U = V - \alpha N^2. \tag{4}$$

Here Eqn. (1) describes fluctuation intensity evolution in terms of growth $(\gamma \sim \nabla_r P \sim N)$, nonlinear transfer to dissipation and electric field shear suppression. Eqn. (1) is a spectrally-integrated wave kinetic equation. Eqn. (2) relates poloidal velocity shear evolution to the Reynolds stress dynamo[13-15] and magnetic pumping induced dissipation. Eqn. (3) relates pressure gradient evolution to particle and heat sources (Q), and fluctuation-induced and neoclassical transport. Eqn. (4) is the ion force-balance equation, which defines the electric field. Here, pressure gradient evolution is taken to be dominated by particle transport. Finally, the dimensionless fields and parameters are defined according to:

$$E = \frac{\alpha_1 E}{\overline{\gamma}_0}, V \equiv \sqrt{\frac{\alpha_2}{\overline{\gamma}_0}}\langle V_E\rangle', U \equiv \sqrt{\frac{\alpha_2}{\overline{\gamma}_0}}\langle V_\theta\rangle', \tau = \overline{\gamma}_0 t,$$

$$a \equiv \frac{\alpha_3}{a_1}, b \equiv \frac{\mu}{\overline{\gamma}_0}, A \equiv \frac{\chi_1}{\overline{\gamma}_0 W_k^2}, \tag{5}$$

$$B \equiv \frac{\chi_0}{\overline{\gamma}_0 L^2}, \overline{Q} \equiv \frac{Q}{\overline{\gamma}_0}, a \equiv \frac{V_i \rho_i}{L^2}\sqrt{\frac{\alpha_2}{\overline{\gamma}_0}}.$$

The parameters $\alpha_1, \alpha_2, \alpha_3$ are derived and tabulated (for various turbulence models) in Table (1) of reference (11).

Eqns. (1-4) correspond to the fluctuation wave kinetic equation, poloidal momentum equation and particle transport equation radially integrated over one turbulence spectrum width. They thus constitute a "single spatial scale" model of L→H dynamics, and are suitable for describing narrow transport barrier evolution characteristic of "standard" H-mode plasmas. Indeed, the width of the barrier in such plasmas is comparable to the width of the turbulence correlation length in L-mode[16]. It should also be noted that the basic structure of these equations is independent of the L-mode turbulence model.

The predictions of this model vis-a-vis the dynamics of E_r' and the evolution of the transition are nicely summarized by Fig. (1), which illustrates the temporal evolution of $\overline{E}, \langle V_\theta \rangle'$ and N, during a "ramp" of power with time (i.e. $\overline{Q} \sim t$). At the L→H transition ($t \sim 200$), a sudden drop in fluctuation intensity is accompanied by rapid growth of $\langle V_\theta \rangle'$. This corresponds to the poloidal velocity dynamo instability, which re-apportions (pressure) gradient free energy between turbulent fluctuations and the mean flow, thus improving confinement. At the same time, the reduction in fluctuation level results in an increase in N, corresponding to a steepening of ∇P due to decreased transport. However, self-consistency ultimately asserts itself! As the fluctuation intensity continues to drop, the Reynolds stress dynamo first saturates, and then $\langle V_\theta \rangle'$ decays rapidly, as the dynamo term no longer exceeds magnetic pumping damping. At the same time N ($\sim \nabla P$) increases rapidly, so that clearly V_d' is the dominant contributor to V_E' in the "time-asymptotic" H-mode state. In this state the fluctuations are quenched.

Several aspects of the evolution described above merit further discussion. First, the model clearly suggests a "two-stage" paradigm for the L→H transition. In the first stage, which occurs for $P \gtrsim P_{thresh}$, the flow dynamo instability is triggered. This results in the growth of poloidal velocity shear and in a moderate reduction in fluctuation level. Note, however, that the fluctuation level must be sufficient to drive the Reynolds stress. In this stage, V_E' is primarily due to V_θ', and the ambient transport is reduced, but not quenched. Hence, there is some constraint upon ∇P-steepening, so that an ELM-free H-mode is possible at modest power. In the second stage, for which $P > P_{thresh}$, the fluctuations are quenched. As a consequence, the poloidal flow decays, and the pressure gradient is the dominant contributor to E_r'. In this stage, the ambient transport is reduced to feeble levels, so that the pressure gradient will surely steepen to the ballooning limit, resulting in the onset of ELMs, which are discussed in Section (IV) of this paper. A second aspect of the evolution is that the ratio of poloidal flow shear to diamagnetic velocity shear is given by

$$\frac{V_d'}{V_\theta'} = \frac{b/a - \overline{E}}{\overline{E}},$$

which further illustrates the dominance of V_θ' near threshold $b/a = \overline{E}$, and the dominance of V_d' at high power $(\overline{E} \to 0)$. A third notable aspect of the evolution is that the temporal duration of the "flow dynamo" phase is sensitive to the rate at which the external power input is "ramped." Specifically, a rapid power ramp will compress the time duration of the flow-dynamo phase, and thus may render it unobservable to diagnostics without sufficient

temporal evolution[17]. Also, as with any bifurcation, the transition time diverges at the power threshold. Thus, the detailed transition dynamics are best studied at modest power levels. A fourth interesting aspect of the model is the fact that the ambient L-mode pressure gradient serves as the "seed" for the transition, by driving a diamagnetic velocity which is amplified by the flow dynamo, once the power threshold is exceeded. The sign of the seed V_E' is determined by the relative magnitudes of L_n and L_{Ti}. For $L_n < L_{Ti}$, the sign is consistent with an inward electric field[18]. The L→H bifurcation is subcritical. Finally, it should be noted that this simple model does not address the phenomenon of "dithering." An improved version, which incorporates explicit correlation time amplitude dependence, clearly manifests dithering and is discussed elsewhere[19].

Two urgent concerns for ITER are the physics and associated parameter scalings of the L→H power threshold. In this model, the threshold is defined by the competition between the flow shear dynamo and magnetic pumping[20]. As the dynamo is fluctuation driven (and thus tied to input power by transport), a power threshold appears straightforwardly. For drift-ITG type turbulence, the ratio of local flow shear drive and damping defines a dimensionless parameter $\rho = (V_{THi}/L_T\mu)(L_n/L_s)(\Delta_r/L_n)^2$. Here Δ_r refers to the fluctuation correlation length, μ to magnetic pumping damping and the other notation is standard. The transition occurs when $\rho > 1$. The physics of the transition is thus clearly revealed to be the condition that the edge gradient steepen to the point that the flow dynamo is triggered. It is interesting to note that $\rho \sim T_i^3/n$, in accord with experimental findings[21]. The condition that $\rho > 1$ may be converted into a power threshold by imposing power balance and utilizing standard drift-ITG transport models. The result is $P_{thresh} \sim (\mu nT)_{edge} aRL_s$. Here $(\mu nT)_{edge}$ is to be evaluated using L-mode edge parameters, just prior to the transition (i.e. μ should be evaluated for plateau or Pfirsch-Schluter conditions). Note that P_{thresh} scales with surface area, and is lower under conditions of strong magnetic shear. Taking $T \sim B_T$ yields a scaling in accord with many experiments.

While this paper is necessarily phenomenological in orientation, two aspects of the theoretical underpinnings of the model merit further discussion here. First, the flow-shear dynamo instability is clear a key ingredient for this L→H transition model. Numerical solution of the primitive equations has verified the existence of the flow dynamo instability[8b,c]. Recent fundamental work[22] on flow shear amplification has adapted methodology from magnetic dynamo theory to the Reynolds dynamo problem. A mean-field flow dynamo is indeed predicted for the Hasegawa-Mima system, but requires a finite $\langle k_\perp^2 \rho_s^2 \rangle$. In particular, for isotropic (but not homogeneous) turbulence spectra, no dynamo is possible in an ordinary 2D-Euler fluid. This finding, confirmed by recent numerical studies[23], establishes that the results of Ref. [13c] are not general and largely a consequence of the specialized initial conditions chosen there. It also suggests that the formation of large scale flows may be related to the presence of finite time singularities in the turbulence. A second theoretical issue is the physics of shear suppression. Clearly, the shear suppression model used here is the simplest one consistent with basic parity symmetry. The model should be extended to include E_r curvature, finite amplitude suppression effects and E_r'-induced wave absorption.

Several rather straightforward extensions to this model should be implemented in order to resolve ambiguous issues. These include:

a.) neutral influx effects, especially the impact of charge exchange on flow damping and thus on the power threshold,

b.) simultaneous evolution of particle and temperature profiles,

c.) the effects of turbulence and E_r' on magnetic pumping damping,

d.) the impact of ballooning fluctuation structure on E_r' evolution,

e.) the sensitivity of P_{thresh} to ion ∇B-drift direction.

These issues will be addressed in future publications.

III.) VH-Mode Evolution

The discovery of the VH-mode[24] is of great significance for two reasons. First, it represents a regime of confinement enhanced beyond H-mode levels. Second, the VH-mode is of scientific importance since it demonstrates that the transport barrier may be significantly delocalized from the plasma boundary. Thus, transport barrier formation and development are almost certainly <u>not</u> related to orbit loss[25] and related effects. This view is supported by recent findings from JT-60U, where the enhanced confinement regime develops in the core and propagates radially <u>outward</u>. Thus, the critical issues related to VH-mode evolution are:

a.) What is the mechanism of VH-mode build-up? How can the spatio-temporal evolution of the transport barrier be described?

b.) What roles do V_θ', V_d' and toroidal rotation $\left(V_\phi\right)$ play in the VH-mode electric field evolution? What controls transport of $\left\langle V_\phi \right\rangle$?

c.) What constitutes the "seed" for the VH-mode electric field? What determines the spatial extent of the enhanced confinement region?

d.) Why are ELMs not observed in VH-mode? What triggers termination of VH-mode?

Recent progress on these issues is discussed below.

The basic model of the L-H transition (Eqns. (1-4) is local, but may be extended to include spatial coupling by retaining radial transport of the local order parameters $\overline{E}$, U and N. At the simplest level, this is accomplished by inserting fluctuation-dependent diffusion into Eqns. (1-3). Thus, the transition model is naturally generalized to:

$$\frac{\partial \overline{E}}{\partial T} - \frac{\partial}{\partial x}\left(\overline{E}\frac{\partial}{\partial x}\overline{E}\right) = \overline{E}N - V^2\overline{E} - \overline{E}^2, \tag{6}$$

$$\frac{\partial}{\partial T}U - \frac{\partial}{\partial x}\left(\overline{E}\frac{\partial}{\partial x}U\right) = a\overline{E}V - bU, \tag{7}$$

$$\frac{\partial N}{\partial T} - \frac{\partial}{\partial x}\left(\overline{E}\frac{\partial N}{\partial x}\right) = -A\overline{E}N - BN + Q, \tag{8}$$

with

$$U = V - \alpha N^2. \tag{9}$$

Here, $x = X/L_\perp$, D_0 is the L-mode diffusively and $L_\perp$ is the gradient scale length in L-mode. Note that the VH-mode model consists of a set of coupled nonlinear reaction-diffusion equations, with field-dependent diffusivities. Such systems are known to exhibit complex evolutionary behavior[26].

Considerable basic insight may be obtained by studying a simplified fluctuation-flow evolution model, which is obtained from Eqns. (6-9) by setting U=V and ignoring N evolution. This model is the spatially non-local analogue of the "predator-prey" L→H transition model advanced in Ref. [11]. This model exhibits a super-critical bifurcation between L-mode-like and H-mode-like states. As with any super-critical bifurcation, the transition occurs via an instability of the L-mode root. This instability occurs in the flow-shear modulation mode, while the fluctuation modulation mode remains heavily damped. Thus, the fluctuation evolution may be "slaved" to flow evolution, described by a single Ginzburg-Landau equation of the form:

$$\frac{\partial}{\partial t} V_\theta' - \frac{\partial}{\partial x}\left[\frac{D_0\gamma_0}{\alpha_1}\left(1-\alpha_2\frac{V_\theta^{2\prime}}{\gamma_0}\right)\frac{\partial V_\theta'}{\partial x}\right] = \gamma_0\Delta\varepsilon V_\theta' - \frac{\alpha_2\alpha_3}{\alpha_1}V_\theta^{3\prime} \tag{10}$$

Here $\Delta\varepsilon = \alpha_3/\alpha_1 - \mu/\gamma_0$ and $\Delta\varepsilon > 0$ is the local super-criticality condition. This equation[27] is similar to the KPP and Fisher equations used to describe epidemic propagation. A leading edge analysis reveals that transition front solutions (i.e. $V_\theta' = V_\theta'(X - V_f t)$) exist and propagate at speed

$$V_f = 2\frac{\Delta_r}{L_\perp}(\gamma_0\Delta_r)(\Delta\varepsilon)^{1/2}. \tag{11}$$

These solutions connect regions with V_θ' finite (i.e. H-mode) with $V_\theta' = 0$ regions. Obviously $\Delta\varepsilon > 0$ is necessary for propagation, i.e. local super-criticality to the L→H bifurcation must be achieved. Note that V_f is not simply due to radial transport, but rather a hybrid process of diffusion $(\gamma_0\Delta_r^2 = D_0)$ and the local L→H bifurcation instability (i.e. $\Delta\varepsilon^{1/2} \sim (P/P_{crit}-1)^{1/2}$). Thus the front propagates <u>into</u> locally super-critical regions. The width of the transition layer[27] (i.e. front width) is given by

$$\Delta X_f \equiv \frac{\Delta_r^2}{L_\perp}(\Delta\varepsilon)^{-1/2} \tag{12}$$

This expression is derived assuming $\Delta X_f > \Delta_r$. ΔX_f is analogous to the phase correlation length in critical phenomena. It should be mentioned that these results are valid for spatially varying $\alpha's$, assuming $\Delta X_f < \left((1/\Delta\varepsilon)|d\Delta\varepsilon/dx|\right)^{-1}$. A typical front is shown in Fig. (2). The analytical results are supported by numerical solutions of the model equations.

In considering the effects of pressure gradient evolution, a qualitative change in the dynamics of propagating transitions occurs. In contrast to the simpler flow-fluctuation model, the L→H transition is locally seeded at all radii by the L-mode pressure gradient (if $\Delta\varepsilon > 0$). Thus, the evolution of the transition at a particular point may occur via an L→H transition front propagating through the region or via a local collapse or quench of the fluctuations and concomitantly abrupt steepening of ∇P. The precise route of transition thus depends on the comparative magnitudes of the poloidal velocity shear and diamagnetic flow shear, with $V_\theta' > V_d'$ indicating a front, and $V_\theta' < V_d'$ corresponding to a "collapse." More precisely, the route to transition is determined by $T_T/T_{f\ell}$, where $T_T = L_\perp/V_f$ is the front transit time and $T_{f\ell}$ is the fluctuation reduction time. In this model,

$$\frac{T_T}{T_{f\ell}} = \frac{1}{2}\frac{L_\perp^2}{\Delta_r^2}\left(a\left(\frac{Q}{A}\right)^{1/2} - b\right)^{1/2}\left\{\ell n\left[\frac{A\left(a^2\frac{Q}{A} - b^2\right)^{1/2}\left(a\left(\frac{Q}{A}\right)^{1/2} - b\right)^{1/2}}{a^{1/2}b^{3/2}\alpha Q}\right]\right\}^{-1} \qquad (13)$$

where $\alpha = \left(c_s\rho_s/L_\perp^2\right)\left(\alpha_2/\bar{\gamma}_0\right)^{1/2}$, and $A = D_0/\bar{\gamma}_0\Delta_r^2$. Note that the extrema $T_T << T_{f\ell}$ and $T_T >> T_{f\ell}$ will appear as a "spatially propagating local" transition and a "global" or "non-local transport" transition, respectively. Spatially propagating "front" and "non-local collapse solutions of Eqns. (6-9) are contrasted in Fig. (3).

Having developed the basic theory of spatio-temporally propagating transition fronts, it is now possible to address the issues concerning the VH-mode raised earlier. First, the VH-mode develops by a spatially propagating (i.e. convective) transition instability. The dynamics of this instability are a hybrid of local transport and the local phase transition instability. Propagation can occur either slowly (i.e. $T_T < T_{f\ell}$), in the form of a localized, but moving, front, or rapidly (i.e. $T_{f\ell} < T_T$) in the form of a "non-local" collapse. Second, both V_θ' and V_d' contribute to the spatio-temporally evolving V_E'. For $T_T < T_{f\ell}$, the electric field is primarily due to rotation. For $T_{f\ell} > T_T$, V_d' dominates. Also, since the spatially localized transition model indicates that the "finite V_θ'" stage is usually of limited duration, it follows that the $V_\theta \neq 0$ layer should appear as an "attached wake," which lags behind (but moves with), the local transition front. In the case of a "non-local collapse," the extent of this V_θ wake shrinks. Thus, detecting poloidal rotation associated with VH-mode evolution is most feasible when $P \gtrsim P_{crit}$, using a multi-channel (in space) CER system. Note that toroidal rotation (V_ϕ) is not apriori necessary for a spatially propagating transition. This is consistent with the fact that a VH-mode like regime has been achieved on TUMAN III[28]. Third, the extent of the enhanced confinement zone is determined by the radial width of the locally super-critical region (i.e. $\Delta\varepsilon > 0$). Note that this criterion naturally favors conditions of modest density and high ion temperature (to minimize magnetic pumping), as well as peaked profiles (to maximize drive). Such conditions are typical of VH-mode discharges. It follows that the VH-mode should develop from the "seed" region to the periphery of the power deposition region.

Regarding the seed, the model predicts that the VH-mode will develop in all regions where $\Delta\varepsilon > 0$ and a finite seed E_r' exists. Thus, "inside-out" development, as recently observed on JT-60U, is consistent with the model and suggests that in such cases, the local core plasma ∇P is the strongest "seed" contributor. Fourth, this model does not explain the absence of ELMs (see Section IV) in VH-mode discharges. This is most likely due to the effect of triangularity, which yields access to the second stability region for ideal ballooning modes[29]. Finally, the VH-mode evolution phenomena discussed here also serve as paradigms for more general manifestations of non-local spatio-temporal transport and propagation phenomena.

To make contact with current experiments, a table of the model predictions for VH-mode evolution in JET and DIII-D is presented in Table 1. Reasonable semi-quantitative agreement is found. In evaluating these predictions, keep in mind that neutral friction is neglected, so that "perfect" wall conditioning is tacitly assumed.

The model discussed above neglects toroidal rotation effects. While V_ϕ evolution is not an absolute necessity for a VH-mode model, toroidal rotation undoubtedly makes a significant contribution to E_r'. Including V_ϕ, the electric-field shearing velocity becomes:

$$V_E' = V_\theta' - \frac{c}{|e| B_T L_n}\left(\frac{dT_i}{dr} - \frac{T_i}{L_n}\right) - \frac{1}{B_T}\left[B_\theta V_\phi' + B_\theta' V_\phi\right]. \qquad (14)$$

Note that V_ϕ enhances V_E' through its own shear and through synergism with the local $B_\theta(r)$ and current density. To calculate the toroidal momentum flux $\Gamma_{P_\phi} = n\left\langle \tilde{V}_r \tilde{V}_\phi \right\rangle + V_\phi \Gamma_n$, it is necessary to evaluate the toroidal Reynolds stress $\left\langle \tilde{V}_r \tilde{V}_\phi \right\rangle$. Using standard a fluid model and quasilinear closure yields:

$$\left\langle \tilde{V}_r \tilde{V}_\phi \right\rangle = -\chi_\phi \frac{\partial V_\phi}{\partial r}$$

$$+ \sum_{\underline{k}} L_{\underline{k}} \rho_i V_{Ti} (k_\theta k_\parallel) V_{Ti}^2 \left| \frac{e\hat{\phi}_{\underline{k}}}{T_i} \right|^2 \left[\chi_{\delta n} + \chi_{\delta T}\right]_{\underline{k}} \qquad (15a)$$

$$+ \frac{B_\theta}{B_T}\left(\chi_\phi \frac{\partial}{\partial r}\left(\frac{c}{B_T}\langle E_r \rangle\right) - \left\langle \tilde{V}_r^E \tilde{V}_\theta^E \right\rangle\right),$$

where

$$\chi_\phi = \sum_{\underline{k}} L_{\underline{k}} \left\langle V_{r,E}^2 \right\rangle_{\underline{k}}. \qquad (15b)$$

The first term on the RHS of Eqn. (15a) corresponds to the (diagonal) momentum diffusivity, first derived by Mattor and Diamond. The second term, due to ion diamagnetic drift effects, is an off-diagonal contribution (pinch), requiring spectral symmetry breaking $\left(\langle k_\theta k_\parallel \rangle \neq 0\right)$. This symmetry breaking may be induced by finite E_r'. Such a term

represents the toroidal momentum flux induced by acoustic wave coupling. The third and fourth terms (also pinch contributions) are due to the ion polarization drift and appear multiplied by $B\theta/B_T$. Throughout, $L_{\underline{k}}$ is the propagator (including E_r') and $\chi_{\delta n}$ and $\chi_{\delta T}$ are the susceptibilities for the non-adiabatic ion density and temperature fluctuations. Thus, a rather detailed theory of V_ϕ evolution is available and can be added to the L→H transition model.

The principal outstanding issues concerning the VH-mode model include:

a.) implementation of the V_ϕ evolution model discussed above in the front paradigm.
b.) treating both particle and heat transport in a 1-D model, including neutral fueling and penetration effects.
c.) including triangularity in the associated ELM model (discussed below).

These issues will be addressed in a future publication.

IV.) Edge Localized Mode (ELM) Dynamics

ELMs[30] are intrinsic constituents of H-mode plasma dynamics. On one hand, ELMs are essential to ash and impurity control. However, the peak heat loads associated with giant ELM bursts severely stress and constrain divertor design and technology. Thus, unraveling the paradoxical nature of ELMs is crucial to a rational design for ITER.

The basic issues of ELM dynamics may be summarized as:

a.) What physics distinguishes the various types of observed ELMs? Can ELMs be classified logically?
b.) How do ELM frequency (ω_E) and ELM-induced energy losses ΔE scale with input power and other control parameters? In particular, what are the requirements for access to grassy ELM regimes?
c.) Is ELM-free operation possible, and how is it achieved? What distinguishes Type -III ELMs from giant and grassy ELMs, and from "dithering?"
d.) Why and how can the observed edge pressure gradient exceed the ballooning limit in H-mode? What role does ballooning instability play in ELM dynamics?
e.) Do ELMs exhibit hysteresis behavior?

The issues are addressed using a "minimal" ELM model discussed below, which is a straightforward extension of the L→H transition model presented earlier in this paper.

The key ingredients in a model of ELMs are a successful L→H transition theory and an understanding of ideal ballooning mode stability in H-mode edge plasma environments. The latter requirement follows from the observation that ELMs seem related to edge-localized MHD activity due to ∇p-proximity to the ballooning threshold[31]. Briefly summarizing, there are four principal effects which enter the determination of ballooning mode stability in an H-mode edge plasma[32]. These are:

i.) electric field shear, which tends to distort fluctuations via differential drifts. This is the strongest effect,

ii.) poloidal angular momentum stratification (i.e. $\left(r^2\Omega_\theta\right)'$), which, as in simple Taylor-Couette flow, may be stabilizing or destabilizing. For the usual ease of an inward electric field $\left(E_r' < 0\right)$, the combination of i.) and ii.) shifts the first stability

boundary toward higher ∇p, consistent with the experimentally observed exceedance of the $(E_r = 0, V_\theta = 0)$ ballooning threshold,

iii.) radial centrifugal force due to rotation, which enhances interchange and ballooning drive,

iv.) Kelvin-Helmholtz (shear flow) drive, which couples to ballooning. This effect is only relevant to regimes of extremely strong velocity shear.

The combined effects (i.)-iv.)) shift and distort the familiar $s-\alpha$ stability diagram. Indeed, such a diagram must now be interpreted as a two-dimensional "slice" through a 3D $s-\alpha-\bar{V}_E'$ stability "solid" ($\bar{V}_E'$ corresponds to a normalized measure of electric field shearing velocity). A set of such modified $s-\alpha$ diagrams is shown in Fig. (4). Note that the magnitude and direction of the shift in the stability boundary is determined by the normalized shearing parameter.

The ELM model may now be straightforwardly constructed. The central idea is that the turbulence and fluctuations consist of two constituents: ε_D, which corresponds to the intensity of ambient drift-ITG modes, and ε_M which corresponds to the intensity of MHD ballooning fluctuations. ε_M responds to violation of the local ballooning instability threshold on time scales which are faster than drift wave decorrelation rates. ε_M "feeds back" on H-mode dynamics via strongly enhanced heat and particle transport and by enhanced poloidal momentum transport (i.e. turbulent viscosity, which damps V_θ'). Note that the equality of (fluid) kinetic and magnetic fluctuation energies intrinsic to (Alfvenic) ballooning modes results in a cancellation between fluid and magnetic Reynolds stress dynamo terms. Thus, the minimal ELM model[33] may be written (in normalized variables) as:

$$\frac{\partial p'}{\partial t} = \Phi - p'\left(\tilde{d}\,\varepsilon_D + \tilde{d}_m \varepsilon_M\right) \tag{16a}$$

$$\frac{\partial V_\theta'}{\partial t} = \varepsilon_D V_E' - \left(\tilde{\mu} + \varepsilon_M\right) V_\theta' \tag{16b}$$

$$\frac{\partial}{\partial t}\varepsilon_D = \gamma_0 (p)' \varepsilon_D - \alpha_1 \varepsilon_D^2 - \alpha_2 V'^2_E \tag{16c}$$

$$\frac{\partial}{\partial t}\varepsilon_M = \tilde{\lambda}\,\varepsilon_M\left(p' - 1 - b\,V'^2_E\right) \tag{16d}$$

$$V_E' = V_\theta' - \tilde{c}\,p'^2 \tag{16e}$$

The notation is discussed in Ref. [33], but the correspondence to the L→H model is obvious. Note that ∇p effects on V_E' may be turned off by $\tilde{c} = 0$. Similarly, V_θ' effects are eliminated by $\mu \to \infty$. In this way, the results (i.e. model ELM history traces) may be compared to experiment in such a way as to elucidate the relative contributions of V_θ' and V_d' to V_E'. Note also that this is a single scale (0-D) model, which treats the entire enhanced confinement zone as a "lump."

The straightforward numerical solution of Eqns. (16a-e) yields interesting results. in Fig. (5) a "trace" plot shows an L→H transition followed by an extended ELM-free period, the duration of which is sensitive to the shape of the power ramp. As ∇p steepens toward ∇P_{crit}, ELMs begin and persist throughout the H-phase. Note that hysteresis of ELM phenomena is exhibited after "power" is reduced to L-phase levels. This familiar type of behavior is exhibited by both the V_θ'-dominated $(\tilde{c}\to 0)$ and ∇p -dominated $(\tilde{\mu}\to\infty)$ models in Figs. (6) and (7), respectively. In Fig. (6), the L→H transition occurs at $t \gtrsim 200$, and an extended ELM-free period persists for $200 < t \le 600$. This is consistent with $V_E' \approx V_\theta'$ saturating ∇p-steepening below the ballooning threshold. At $t \ge 600$, the power is ramped up further, leading to the onset of ELMs. Here, ELMs appear as ∇p sawtooth oscillations (obviously, $\nabla p \sim \Delta E$), bursts of MHD activity, and sawteeth in V_θ'. In Fig. (7), the L→H transition occurs at $t \sim 75$, and ELMs begin almost immediately. This is a consequence of the fact that $V_E' = V_d'$, so in this case ∇p must steepen considerably for the transition to occur. A comparison of Figs. (6), (7) then suggests that extended ELM-free periods, Type-III behavior, etc. are related to the role of rotation in the transition. Note also that as P_{input} rises at $t \sim 150$ in Fig. (7), evolution from "giant" to "grassy" behavior occurs, in that ω_E increases and p' oscillations drop.

The ELM frequency (ω_E), MHD fluctuation level, and burst magnitude ΔE are plotted vs. P_{in} for the $V_\theta' \cong V_E'$ and $V_d' \cong V_E'$ models, respectively, in Figs.(8) and (9), respectively. Note that both models clearly manifest a trend to evolve from giant and grassy ELMs at high P_{in}. Specifically, $\omega_E \sim P_{in}$ while $\Delta E \sim P_{in}^{-1}$ so that $\omega_E \Delta E$ is roughly constant. This behavior is a simple (but important!) consequence of the increasingly "tight" marginality to the ballooning limit at high power, and is in excellent agreement with experimental findings[34,35]. However, the $V_E' \simeq V_\theta'$ model predicts a "sagging belly" to the $\omega_E(P_{in})$ curve, while the $V_E' \simeq V_d'$ model predicts an approximately linear rise of ω_E with P_{in}. The latter is more consistent with experiment, and confirms our expectation that ∇p will dominate E_r at high power. The more interesting contrast between Figs. (8) and (9) appears at low and modest power, and suggests that plasma mass flow dynamics may play an important role in ELM dynamics, there. Specifically, while Fig. (9) $\left(V_E' \sim V_d'\right)$ predicts a simple linear $\omega_E(P)$, Fig. (8) $\left(V_E' \sim V_\theta'\right)$ indicates that ω_E rises more slowly than linear. (The initial rise in ω_E is due to transport-induced oscillations, which are an artifact of the model.) In this regime of P_{in}, ΔE rises and ultimately reaches a maximum. The interval $.5 < P_{in} < .7$ of Fig. (8) thus seems to resemble "Type-III" ELM behavior, followed by a transition to Type I, giant ELMs. The rather obscure and somewhat elusive Type-III ELM is a flora best identified by its $d\omega_E/dP_{in} < 0$ branch. Thus, this sojourn through the botanical garden of ELMs may be summarized (in terms of a P_{in}-scan) as:

a.) for $P_{in} \gtrsim P_{thresh}$, dithering may be present, but true ELMs do not occur,

b.) at slightly higher power, "Type-III" ELMs (with $d\omega_E < dP_{in} < 0$ appear. The dynamics of poloidal mass flow appear crucial to the cultivation of Type-III ELMs.

c.) for yet higher power, giant ELMs (Type I) sprout vigorously. A continuous transition from giant to grassy (Type II) ELMs then tracks further increases in P_{in}. In this interval, $V_E' \sim V_d'$ and $\omega_E(P_{in})$ rises linearly, with $\omega_E \Delta_E \sim$ const..

Sample traces of Type III, I, and II ELMs are given for the $V_E' \sim V_\theta'$ and $V_E' \sim V_d'$ models, respectively, in Figs. (10-12) and Figs. (13), respectively. Note that the $V_E' \sim V_d'$ model does <u>not</u> exhibit Type-III ELMs or an extended ELM-free period after the L→H transition, for the parameters chosen. Finally, it is amusing to note that simple concepts such as ideal ballooning stability and the L→H model can semi-quantitatively reproduce the entire botany of ELMs, without the need for a garden of exotic flora such as resistive ballooning, surface kinks, tearing modes, bootstrap-current driven islands, etc..

While the study of ELM dynamics is necessarily a computational endeavor, two aspects of the ELM-paradigm described above merit more detailed, analytical investigation. The first issue concerns "Type-III" ELM behavior-specifically, why does ω_E drop with P_{in} at low powers? This question may be answered by linearizing Eqn. (16) around the ELMing H-mode state, slaving ε_D to V_θ'. Thus:

$$\frac{\partial}{\partial t}\delta p' = \delta V_\theta'^2 \delta p - \tilde{d}_m \delta \varepsilon_M \tag{17a}$$

$$\delta V_\theta'^2 + \delta \varepsilon_M \cong 0 \tag{17b}$$

$$\frac{\partial}{\partial t}\delta \varepsilon_M = \lambda \varepsilon_M^{(0)} \delta p' + \lambda (\delta \varepsilon_M)(\delta p') \tag{17c}$$

Here, $\tilde{\mu}$ has been neglected in comparison to the MHD turbulence viscosity. Eqns. (19a-c) may then be straightforwardly combined to obtain:

$$\frac{\partial^2}{\partial t^2}\delta p' + \omega_E^2 \delta p' + \lambda \delta p' \frac{\partial}{\partial t}\delta p' = 0 \tag{18}$$

where $\omega_E^2 = (\tilde{d} + \tilde{d}m)\lambda \varepsilon_M^{(0)}$ is the unperturbed ELM frequency. Note that ω_E is small at low P_{in}, since $\varepsilon_M^{(0)}$ is small. More interestingly, the $\lambda \delta p(\delta \dot{p})$ term appears as an ELM-amplitude-dependent "friction" $(\gamma_{diss} \sim \lambda \delta p)$, which necessarily forces ω_E to <u>decrease</u> with increased power. This is characteristic of Type-III ELM behavior. In physical terms, as power increases, ε_M increases and exceeds $\tilde{\mu}$ Thus, V_θ' drops more precipitously at an ELM sawtooth "crash." Since the flow shear decays further, the recovery time must also increase correspondingly, resulting in a lower ELM frequency. Note that poloidal flow shear is crucial to this scenario, thus indicating that the "Type-III" phase ends when $V_d' > V_\theta'$.

A second question, of great practical importance, concerns the accessibility of the grassy ELM regime. First, it should be noted that Type-III ELMs are <u>not</u> grassy (i.e. ΔE is <u>not</u> small), so one must traverse the forest of Type-III and giant ELMs in order to graze

peacefully in the high P_{in} grasslands. Specifically, since Type-III ELMs have large burst amplitude, exploiting an ELM-free interval above P_{thresh} seems unfeasible. Indeed, the existence and relevance of such an interval are quite sensitive to parameters. Such regimes are quite likely to be polluted by "dithering," as well. Thus, the threshold power for grassy ELM operation is straightforwardly given by the P_{in} level required for "tight" marginality to ballooning. This in turn implies that (from a standpoint of practical utility) the question of "What is the L→H power threshold?" should be supplemented by the further question, "How far above the transition threshold must one go in order to get grassy ELMs?". The answer to the second question is given by the parameter $\Delta P/P_{LH} = (P_{ball} - P_{LH})/P_{LH}$. Here P_{ball} is the power for ballooning marginality and P_{LH} is the L→H transition power. Straightforward calculations (using plateau regime μ) yield $\Delta P/P_{LH} \sim \beta_{\theta_{edge}}^{-1}\left(\hat{s}^2/4\varepsilon_T^3 q\right)$ for the $V_E' \sim V_\theta'$ model and $\Delta P/P_{LH} \sim \left[\beta_{\theta_{edge}}\left(\varepsilon_T^2/2\hat{s}\right)\left(R/\sqrt{\rho_s L_n}\right)\right]^{-\delta}$, where $2 < \delta < 4$, (depending on modelling assumptions) for the $V_E' \sim V_d'$ model. In both cases, $\Delta P/P_{LH}$ increases strongly with decreasing edge β_θ, and increasing aspect ratio. The implied sensitivity of ELM-type to plasma current (at fixed power) is very clearly observed in experiment[36]. In all cases considered by these authors, $\Delta P/P_{LH} \gtrsim 2$.

Several issues related to ELM physics must still be addressed. Most prominent among these are:

a.) the 1-D structure of ELMs-i.e. how much of the enhanced confinement layer is lost in a burst? This is likely determined by transport dynamics and by magnetic structure and topology.
b.) the effects of shaping, most notably triangularity.
c.) the possible role of surface kinks and bootstrap-current-driven modes, particularly in "second stable" ballooning regimes.
d.) the continued investigation of ELM dynamics near threshold.

V.) Generation of Sheared Plasma Rotation Using Externally Launched RF Waves

Since the L→H transition is accompanied by the formation of a radial electric field in the periphery, a natural question arises as to whether the electric field can be controlled by external means. One potential candidate is the radio frequency wave, which is already employed in heating and current drive. RF is a natural candidate because of its non-perturbative nature, easy control of the resonance location, possible synergistic effects with other uses. We present two related scenarios for electric field generation and discussion of experimental results. The first is the ion Bernstein wave[37], for which recent PBX-M results indicate an RF induced transport barrier. The second involves using fast waves[38].

a.) IBW Flow Drive

In previous work[37], ion Bernstein waves were found to be capable of inducing a radial electric field via poloidal shear flow. The edge localized radial electric field was found to point inward, independent of any controlling mechanism. Thus, a radial electric

field is always expected during heating. Using a slab model, with magnetic field in the $\hat{z}$ direction, the flow gradient generated by IBW was found to be

$$\langle E_r \rangle \equiv \frac{B\phi c_s^2}{C\mu_\theta} \sum_k \left|\frac{e\phi}{T_e}\right|^2 k_\perp^R \left(\frac{\omega \Omega_{ci}^3}{\omega^2 - \Omega_{ci}^2} \left(k_\perp^R \rho_s\right)^2 \right) \times \exp\left(-\frac{\delta_e k_\perp^R (r - r_s)}{2} \right). \tag{19}$$

This flow corresponds to a torque of $T_{ext}^{'} = \mu V_\theta^{'}$. We note that this is the dominant contribution to the poloidal flow, which is due to Reynolds stress, i.e. momentum transport. Based on the BDT model, the required power to suppress fluctuations is

$$P_{abs} > \frac{(\Delta\omega)\mu_\theta T_e^2 \omega_{pe}^2 k_\parallel^2 \delta_e k_\perp^R L_n}{8\pi k_\perp^{R3} \bar{k}_\theta \Delta c_s^2 \omega^2 \Omega_{ci}^2 \left(k_\perp^R\right)^2 |e|^2}. \tag{20}$$

For use below, we define $P > P_0$ where P_0 is the right hand side of the equation above. Using PBX-M parameters, ion Bernstein Waves require relatively low power (~100KW) to suppress fluctuations.

Still more recent work[39] has suggested that the above power estimate is somewhat low. Specifically, the RF drive Reynolds stress, proportional to the RF absorbed power, must exceed a critical parameter, which is in turn dependent on how far one is away from the L→H power threshold. In addition, the radial electric field (near torque-free threshold) is proportional to the one third power of the wave-driven Reynolds stress. We note that in the case of IBW, heating and radial electric field are likely to occur simultaneously. Since the torque necessary for L→H transition depends on heating power away from threshold, the IBW case is more involved, with heating playing a role far from threshold and radial electric field drive playing a role near threshold. Using the results of Newman, et. al.[40], and letting the non-self-consistent power for suppression be P_0, the RF power necessary to suppress the turbulence is

$$P_{rf} > P_0 \frac{2}{3\sqrt{3}} \frac{1}{k_\theta \Delta_x} \left| 1 - \frac{P_{th}}{P_{heat}} \right|^{3/2} \frac{P_{heat}}{P_{th}}, \tag{21}$$

where, P_{heat} is the input (auxiliary) power and P_{th} is the threshold power (defined above, without external torque). Here, k_θ and Δ_x are the rms poloidal wave number and radial correlation length in L-mode, respectively. Typically, for drift waves, $k_\theta \Delta_x \sim 1$. We note that the above condition applies to any external torque gradient, where $T_{ext}^{'}[P_0] \sim \Delta\omega\mu / k_\theta \Delta_x$ where P_0 is the power necessary to drive $T_{ext}^{'}$. Typically, $P_0 \sim T_{ext}^{'}$. Crude estimates of this IBW power (assuming we are away from spontaneous threshold) give about 400KW.

Turning to the experiment, PBX-M observed a core transport barrier during IBW heating. Such a barrier is consistent with the formation of an edge radial electric field. Evidence to suggest this include the observation of barrier formation when a core resonance is present and density peaking at this resonance. These results are consistent with the theory, including the ~ 600KW of IBW power.

b.) Fast Wave Flow Drive

In this section, we will consider plasma flow drive using externally launched fast waves. We choose this fast wave as means of flow drive because first of all, as a mature technology, the fast wave has been used in many tokamaks around the world as a source of plasma heating and current drive. It is also proposed to be used in ITER. Secondly, toroidal plasma rotation has been observed in a recent TFTR ICRF experiment[41]. Third, the fast wave flow drive has the merit that both the flow location and width can be easily controlled externally.

The theoretical analysis of the poloidal and toroidal flow drive in a tokamak using the externally launched fast waves has been carried out[42, 43]. In the following, the results from these analysis will be described.

i.) Poloidal Flow Drive

The basic model of plasma poloidal flow drive is that of a poloidal momentum balance equation:

$$\rho_m^T\left\{\frac{\partial}{\partial t}\langle\tilde{V}_\theta\rangle+\langle\tilde{V}\cdot\nabla\tilde{V}_\theta\rangle\right\}=\langle\tilde{\rho}_q^T\tilde{E}_\theta\rangle+\frac{1}{c}\langle(\tilde{J}\times\tilde{B})_\theta\rangle-\nu_p\langle V_\theta\rangle \qquad (22)$$

where $\langle V_\theta\rangle$ is the mean poloidal flow, $\tilde{E}$ and $\tilde{B}$ are the fluctuating electromagnetic fields of the fast wave, $\tilde{v}$ and $\tilde{J}$ are the fast wave induced fluctuating plasma flow and current. From Eqn. (22), we see that the plasma poloidal flow is driven by a nonlinear inertial force (Reynolds Stress), the electromagnetic force and damped by a poloidal damping (ν_p) due to the poloidal variation of the equilibrium magnetic field in a tokamak. The nonlinear inertial and the electromagnetic force are determined by spatial variations in the fast wave electromagnetic field (pondermotive force). In a two component plasma with low minority ion concentration, rapid spatial variation of the fast wave electromagnetic field occurs across the minority ion resonance layer. As a result, localized plasma poloidal flow can be generated. The flow is localized near the minority ion resonance point $R_0\left(\omega=\Omega_i^m(R_0)\right)$ and has a width of the minority ion resonance layer width, i.e. $\Delta x=R_0(k_\parallel v_i/\omega)$. Since $\Delta x\sim\sqrt{T_i}$, the poloidal flow drive is more effective near the edge of a tokamak where the plasma temperature is lower.

Various forces in Eqn. (22) can be calculated using hot plasma kinetic theory[44]. For example, the fluctuating plasma flow can be expressed as $\tilde{v}=(c/B)M\cdot E$ where M is the hot plasma mobility tensor; the fluctuating plasma current can be expressed as $J=-(i\omega/4\pi)(K-1)\cdot E$ where K is the hot plasma dielectric tensor. At steady state, the total force is balanced by the poloidal damping term. As an example, we have calculated the spatial profiles of poloidal flow velocity at steady state V_θ and its shear dV_θ/dr for a TFTR edge like plasma. The parameters used are: major radius $R=245cm$, minor radius $a=85cm$, magnetic field $B_0=4T$, plasma temperature $T=400eV$, plasma (deuterium) density $n_D=10^13cm^{-3}$, minority ion (hydrogen) concentration $n_H/n_D=1\%$, fast wave frequency $f=46.7MHz$, parallel wavenumber $k_\parallel=0.075$. The results are shown in Figs. (14) and (15) respectively.

Having obtained the spatial profiles of the poloidal velocity and its shear, we can estimate the power needed for suppression of edge turbulence. The criterion for turbulence suppression is that the shearing rate of the flow is larger than the turbulent decorrelation

rate: $\Delta x_k \frac{d}{dx}\langle V_\theta \rangle > \Delta \omega_k$. Using edge turbulence parameters, and the results above, we find that the critical power level is $P_c \simeq 450 KW$. The fact that this number is substantially smaller than what is typically used in most of the current ICRF heating experiment indicates the practical feasibility of using fast wave as a means of flow drive in a tokamak.

ii.) Toroidal Flow Drive

The model for fast wave toroidal flow drive is that of a toroidal momentum balance equation:

$$\left\{\frac{\partial}{\partial t}\langle V_\phi \rangle + \left\langle \tilde{V} \cdot \nabla \tilde{V}_\phi \right\rangle\right\} = \left\langle \tilde{\rho}_q^T \tilde{E}_\phi \right\rangle + \frac{1}{c}\left\langle \left(\tilde{J} \times \tilde{B}\right)_\phi \right\rangle + \mu_\phi \frac{d^2}{dr^2}\langle V_\phi \rangle, \qquad (23)$$

where $\langle V_\phi \rangle$ is the mean toroidal flow, μ_ϕ is the anomalous diffusion rate, while the rest of the terms have the same meaning as they appear in Eqn. (22). Unlike the plasma poloidal flow, the plasma toroidal flow does not suffer from poloidal damping. Instead, it suffers from an anomalous diffusion process. As a result, the toroidal flow generated will not be localized near the spatial position of momentum input (minority ion resonance layer). it will diffuse out to other parts of a tokamak and has a very broad spatial profile. The various forces appearing in Eqn. (23) can be calculated in the same way as the forces in Eqn. (22) are calculated. The steady state toroidal flow profile can be obtained by balancing the total force with the anomalous diffusion term.

We have calculated the spatial profile of plasma toroidal flow at steady state using parameters employed in a recent TFTR ICRF experiment, namely, plasma temperature T = $10 KeV$, plasma density $n_D = 10^{13}$, magnetic field $B_0 = 4T$, wave frequency $f = 61 MHz$, toroidal wavenumber $n_\phi = 14$, hydrogen minority concentration $n_H/n_D = 3\%$, a total $2MW$ of power is deposited on the magnetic axis, and we assume $\mu_\phi = 10^4 cm^2/s$. The result is shown in Fig. (16). The peak magnitude of the toroidal flow velocity of $30 Km/s$ is close to the $20 Km/s$ which is what has been observed in the experiment.

VI. Unresolved Issues

Several unresolved issues cut across the topical boundaries set up in this paper. These include:

a.) determining the radial width of the enhanced confinement layer and ELM burst region. Eqn. (12) gives a promising suggestion, but further work is required.

b.) a systematic means for relating edge parameters to "machine variables." This requires both core and SOL transport analysis.

c.) further confinement regimes, such as the PBX IBW-driven CH-mode. In particular, such experiments should investigate power scaling requirements, artificial ELMs (via external power modulation) and synergisms with the spontaneous H-mode. Indeed, it may be more effective to operate ITER in an L-mode supplemented by externally driven and modulated counter-flow shear layers than in a spontaneous H-mode.

Work on these issues is in progress.

Acknowledgments

We thank Keith Burrell and Marshall Rosenbluth for many helpful, stimulating, provocative and entertaining discussions. This research was supported by the U.S. Department of Energy.

References

[1] WAGNER, F., et. al., Phys. Rev. Lett. 49, 1408 (1982).
[2] PERKINS, F.W., et. al., Paper E-1-I-3, IAEA Proceedings (1994).
[3] JACKSON, G.L., et. al., Phys. Rev. Lett. 67, 3098 (1991).
[4] CRADDOCK, G.G. and DIAMOND, P.H., Phys. Rev. Lett. 67, 1535 (1991).
[5] ONO, M., et. al., IAEA- A-3-5-7, these Proceedings (1994).
[6] BIGLARI, H., DIAMOND, P.H., TERRY, P.W., Phys. Fluids B2, 1 (1990).
[7] DIAMOND, P.H., et. al., IAEA Proceedings 1992, Vol. 2, 97 (1993).
[8] CARRERAS, B.A., et. al., Phys. Fluids B4, 3115 (1992).
CHARLTON, L., et. al., Phys. Plasmas **1**, 2700 (1994).
CARRERAS, B.A., et. al., *Submitted to Phys. Plasmas* (1994).
[9] SIDIKMAN, K., et. al., Phys. Plasma 1 1142 (1994).
[10] GROEBNER, R.J., Phys. Fluids B5, 2343 (1994).
[11] DIAMOND, P.H., et. al., Phys. Rev. Lett. 72, 2565 (1994).
[12] CARRERAS, B.A., et. al., Phys. Plasmas, *In Press* (1994).
[13] DIAMOND, P.H. and KIM, Y.B., Phys. Fluids B3, 1626 (1991).
CARRERAS, B.A., et. al., Phys. Fluids B3, 1438 (1991).
DRAKE, J.F., et. al., Phys. Fluids B4, 488 (1992).
[14] DIAMOND, P.H., et. al., IAEA Proceedings 1992, Vol. 2, 97 (1993).
[15] GRUZINOV, A.V., DIAMOND, P.H., LEBEDEV, V.B., Phys. Plasmas, *In Press* (1994).
[16] DOYLE, E.J., RHODES, T., et. al., IAEA Proceedings, Vol. 1, 235 (1993).
[17] BURRELL, K., et. al., IAEA-A-2-I-5, these Proceedings (1994).
[18] GROEBNER, R.J., et. al., Phys. Rev. Lett 64, 3015 (1990).
[19] GARCIA, L., et. al., IAEA-D-P-1-12, these Proceedings (1994).
[20] DIAMOND, P.H., et. al., Phys. Rev. Lett. 72 (1994).
[21] BURRELL, K., et. al., IAEA Proceedings (1992).
[22] GRUZINOV, A.V., DIAMOND, P.H., LEBEDEV, V.B., Phys. Plasmas, *In Press* (1994).
[23] SOLOVIEV, G., et. al., *Submitted to Phys. Plasmas* (1994).
[24] JACKSON, G.L., et. al., Phys. Rev. Lett. 67, 3098 (1991).
[25] SHAING, K.C. and CRUME, E.C., Phys. Rev. Lett. 63, 2369 (1989).
[26] MURRAY, J.D., "Mathematical Biology," Spring Verlag (Berlin) 1989.
[27] DIAMOND, P.H., et. al., *Submitted to Phys. Plasmas* (1994).
CARRERAS, B.A., et. al., Plasma Phys. and Contr. Fusion 36, Supp. 7(A), 93 (1994).
[28] LEBEDEV, S., GOLANT, V.E., Private Communication (1993).
[29] BURRELL, K., Private Communication (1994).
[30] ASDEX Team, Nucl. Fus. 29, 1959 (1989).
[31] GOHIL, P., et. al., Phys. Rev. Lett. 61, 1603 (1988).
[32] MEDVEDEV, M., and DIAMOND, P.H., *Submitted to Phys. Plasmas* (1994).
[33] LEBEDEV, V.B., et. al., *Submitted to Phys. Plasmas* (1994).
[34] BURRELL, K., et. al., Plasma Phys. Contr. Fusion 31, 1649 (1989).
[35] OSBORNE, T., et. al., H-mode Workshop (1991).
[36] SCHISSEL, D.P., et. al., Nucl Fusion 31, 73 (1991).
[37] CRADDOCK, G.G., DIAMOND, P.H., ONO, M., and BIGLARI, H., Phys. of Plasmas **1**, 1944 (1994).
[38] GANG, F.Y., Phys. Fluids B5, 3835 (1993).
[39] DIAMOND, P.H., et. al., Phys. Rev. Lett., 72, 2565 (1994).
[40] NEWMAN, D.E., et. al., *Submitted to Physics of Plasmas* (1994).
[41] PORKOLAB, M., Private Communication (1994).
[42] GANG, F.Y., Phys. Fluids B5, 3835 (1994).
[43] GANG, F.Y., "Fast wave toroidal flow drive in a tokamak plasma," *In Preparation for Submittal to Physics of Plasmas.*
[44] STIX, T.H., "Theory of Plasma Waves," McGraw-Hill, New York, 1962.

FIGURE CAPTIONS

Figure 1: Power increasing with time, showing onset and saturation of Reynolds dynamo followed by fluctuation quench.

Figure 2: Poloidal velocity shear profiles showing transition front propagation.

Figure 3: Comparison of $T_T << T_{f\ell}$ front propagation and $T_T >> T_{f\ell}$ collapse limits.

Figure 4: $s-\alpha$ diagram including sheared rotation.
Curve 1: static plasma. Curve 2: Solid body rotation enhances drive.
Curve 3: $S_\Omega = -10\left(S_\Omega = (r/\Omega)(d\Omega/dr)\right)$ indicates shear suppression.
Curve 4: $S_\Omega = -5$ indicates weaker shear suppression.
Curve 5: $S_\Omega = 5$ indicates enhanced growth due to poloidal angular momentum stratification. Near origin, Kelvin-Helmholtz modes appear.

Figure 5: ELM model trace indicating L→H transition, ELM-free period, ELMs and hysteresis. A slow power ramp extends the ELM-free phase.

Figure 6: L→H transition and ELMs for $\tilde{c} = 0$ model.

Figure 7: L→H transition and ELMs for $\tilde{\mu} \to \infty$ model.

Figure 8: ELM frequency, MHD fluctuation level and ΔE vs. P_{in} for $\tilde{c} = 0$ model.

Figure 9: As above, for $\tilde{\mu} \to \infty$ model. The discontinuity at $P \cong 2$ is a model artifact.

Figure 10: $\tilde{c} = 0$ model Type III ELMs.

Figure 11: $\tilde{c} = 0$ model Giant ELMs

Figure 12: $\tilde{c} = 0$ model Giant → Grassy evolution with increased power.

Figure 13: $\tilde{\mu} \to \infty$ model Giant → Grassy evolution with increased power.

Figure 14: The spatial profile of poloidal flow velocity V_θ in arbitrary unit. The dotted line indicates the spatial position of minority ion resonance.

Figure 15: The spatial profile of poloidal flow velocity shear dV_θ/dr in arbitrary unit. The dotted line indicates the spatial position of minority ion resonance.

Figure 16: The spatial profile of the toroidal flow velocity V_ϕ. The dotted line indicates the spatial position of magnetic axis.

TABLE I

Input data:

DIII-D: $I_p = 1.0\ MA,\ B_T = 1.2\ T$

$(T_i)_{edge} = 120\ eV$ $(n_e)_{edge} = 1\text{x}10^{13} cm^{-3}$ $L_p/edge = 2.7\ cm$

$\chi_e/edge = 2\text{x}10^4\ cm^2/\text{sec}.$ $W = 1\ cm$ Power = 3 MW
$L_s = 180\ cm$

JET: $(T_i)_{edge} = 400\ eV$ $(n_e)_{edge} = 1\text{x}10^{13}$ $L_p/edge = 2.7\ cm$

$L_s = 360\ cm$ $\chi_e/edge = 4\text{x}10^4$ $W = 1\ cm$ Power = 3 MW

	Transition Time*	Power threshold	Front propagation velocity
DIII-D	$4.7ms$	$2.6Mw$	25 *m/sec.*
JET	$2.6ms$	$2.3Mw$	47 *m/sec.*

*Transition time is the rise time of shear flow, not the fluctuation quench time.

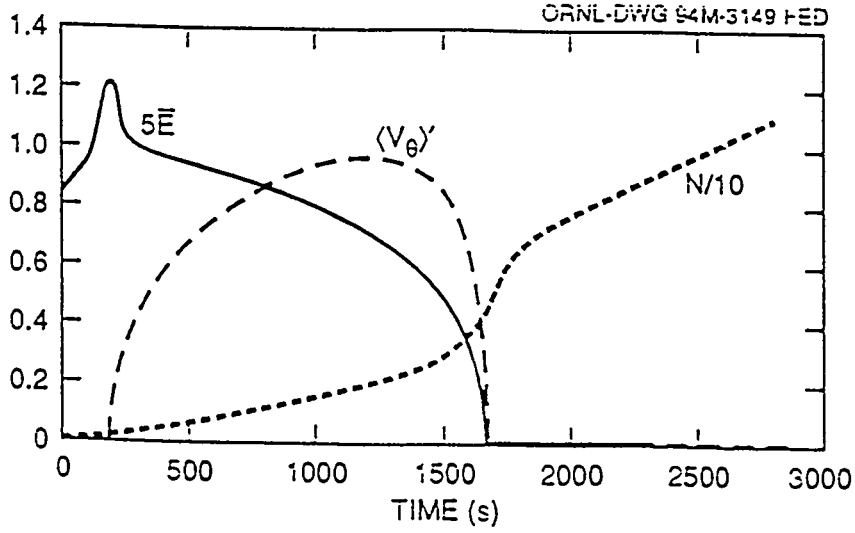
ORNL-DWG 94M-3149 FED
1.4
1.2
1.0
0.8
0.6
0.4
0.2
0
5Ē
⟨Vθ⟩'
N/10
0
500
1000
1500
2000
2500
3000
TIME (s)

Fig. 1

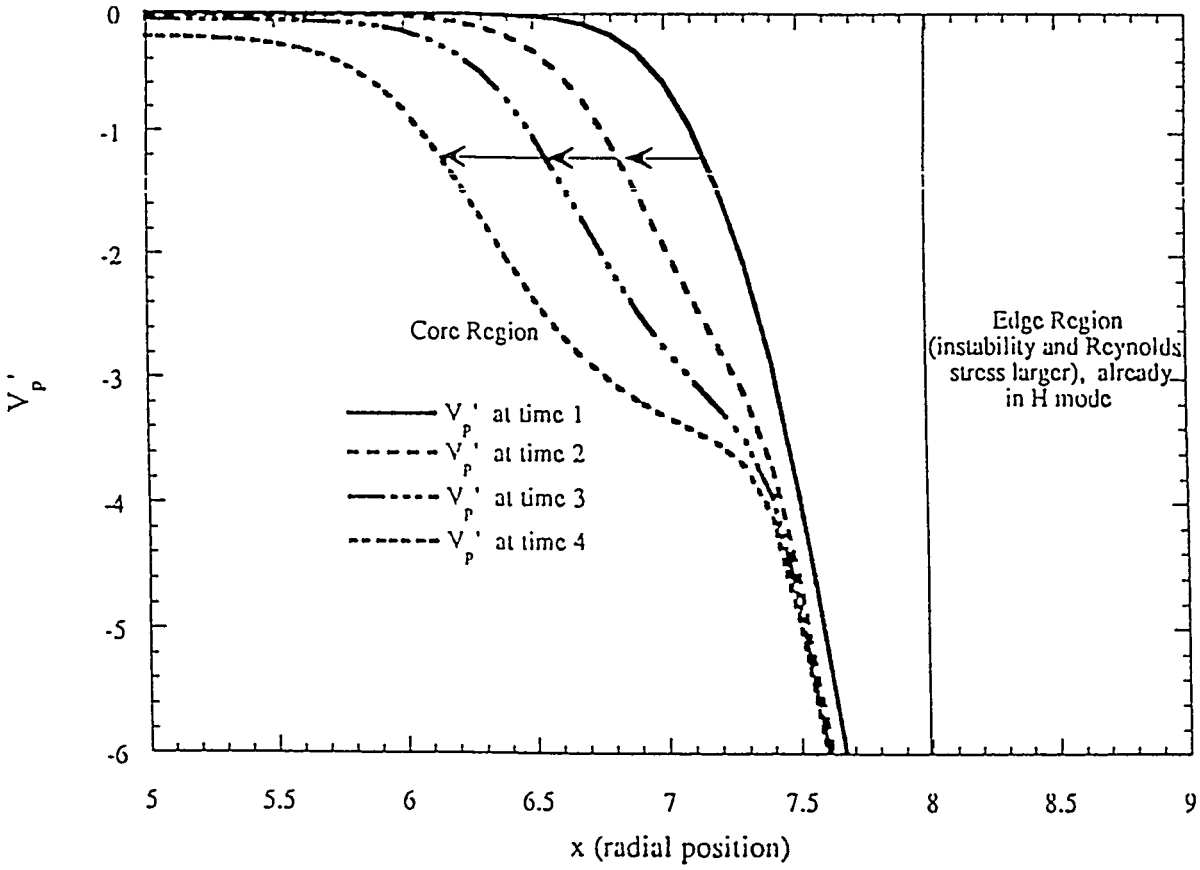
0
-1
-2
-3
-4
-5
-6
V_p'
5
5.5
6
6.5
7
7.5
8
8.5
9
x (radial position)
Core Region
Edge Region
(instability and Reynolds stress larger), already in H mode
V_p' at time 1
V_p' at time 2
V_p' at time 3
V_p' at time 4

Fig. 2

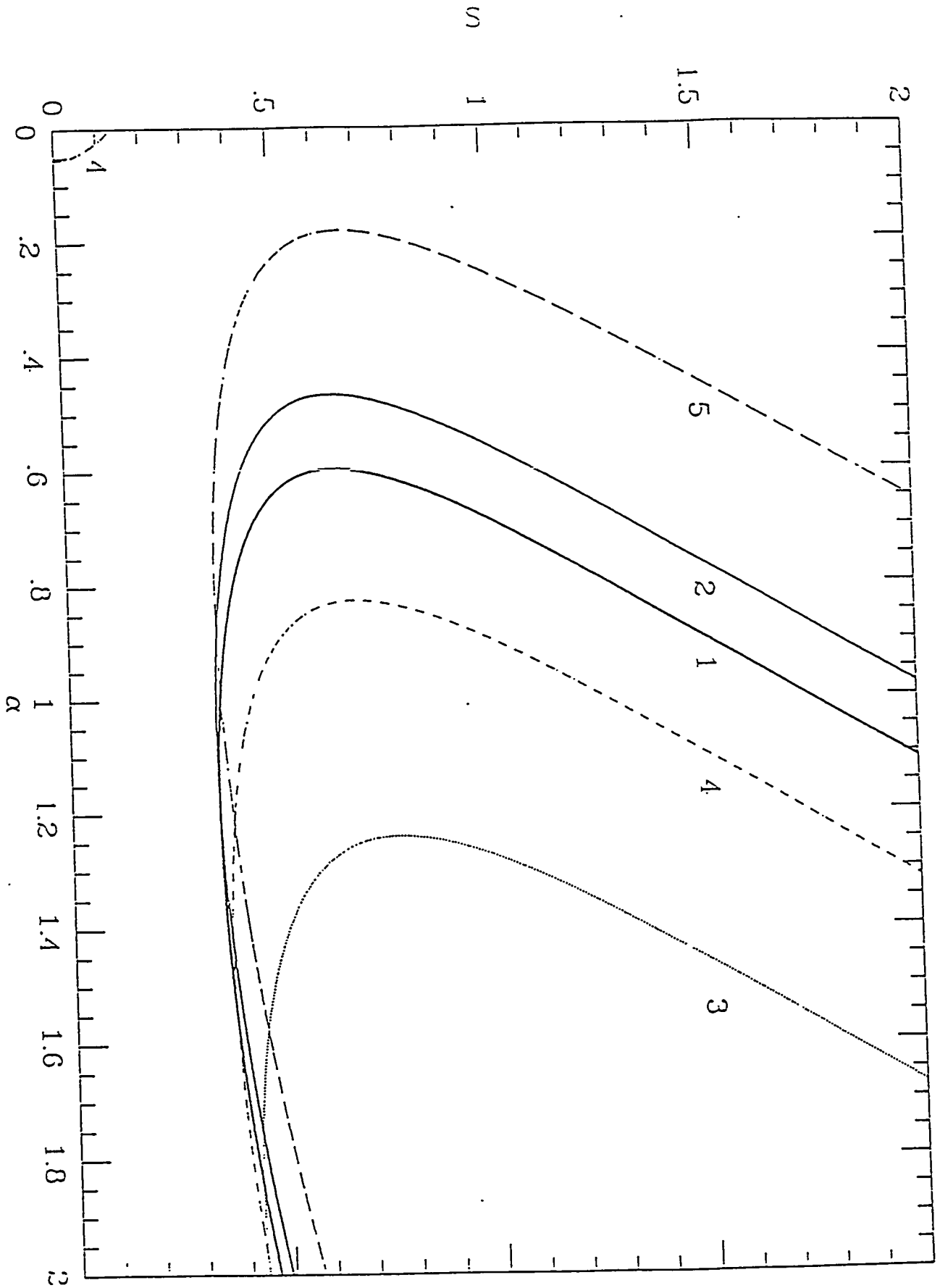

Fig. 4

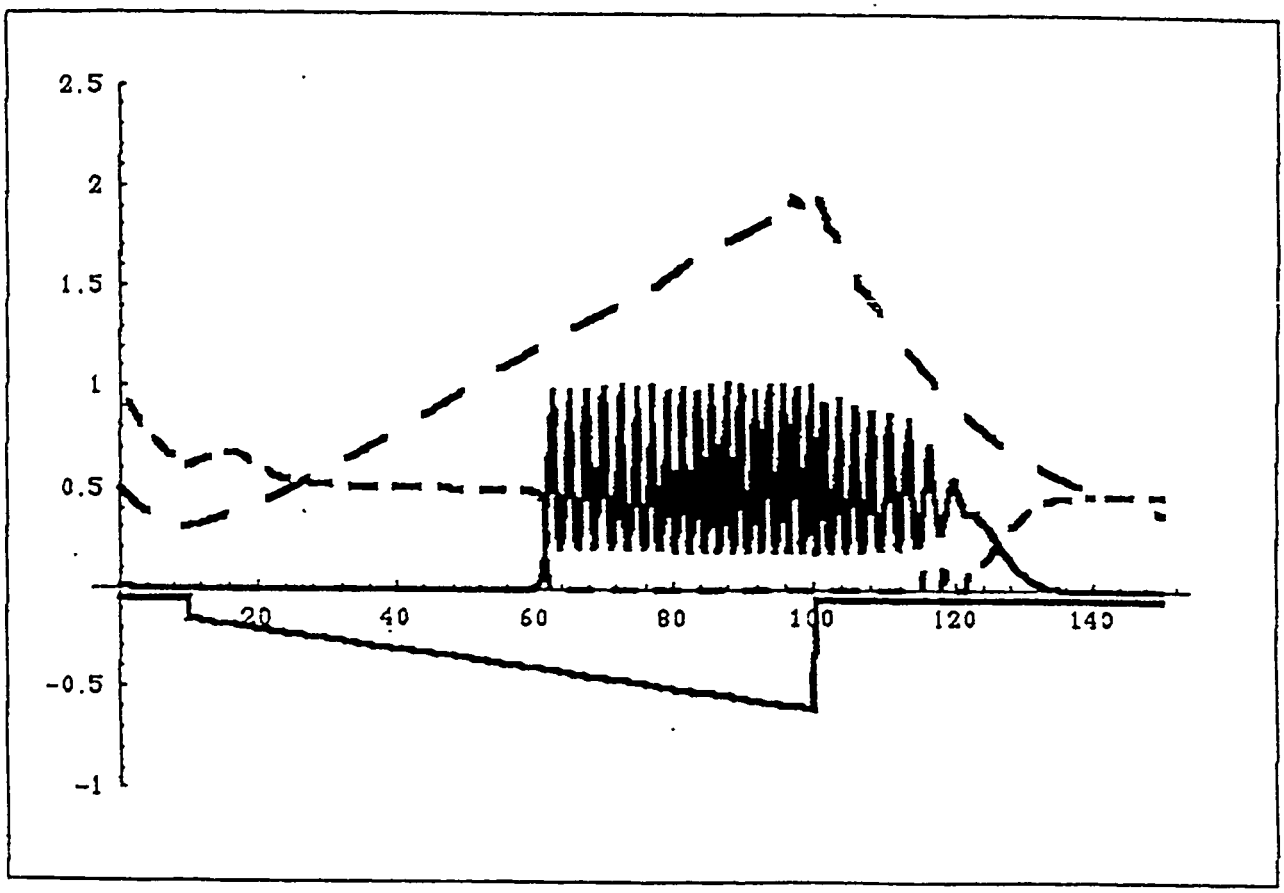

Fig. 5

Input power

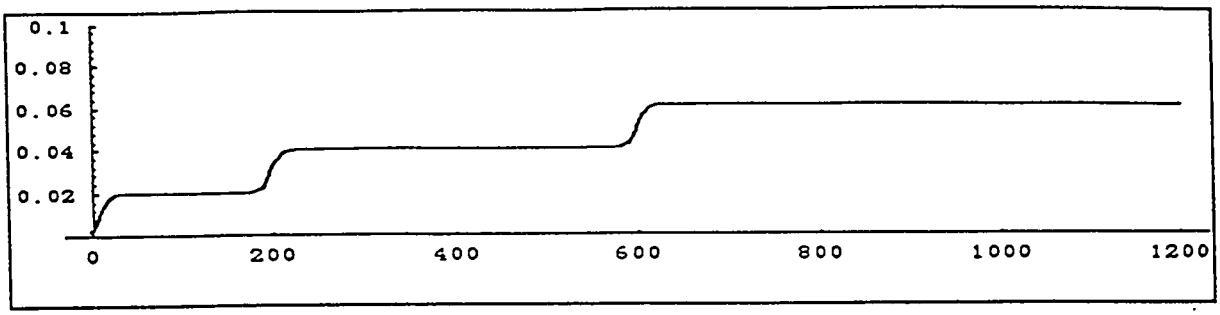

Pressure gradient

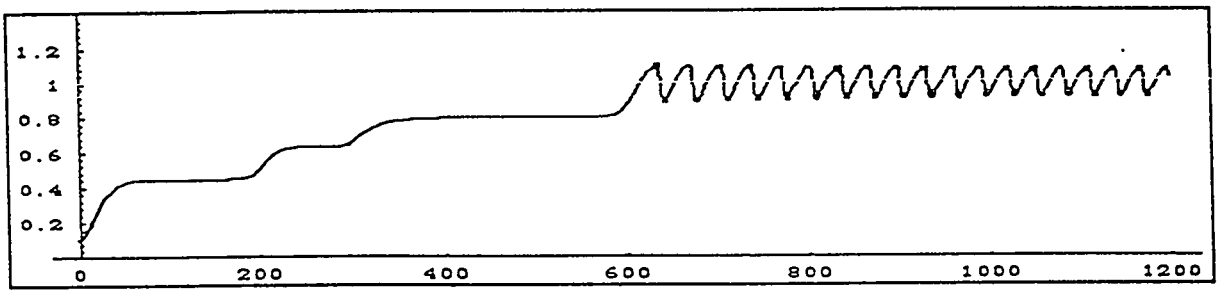

MHD fluctuations

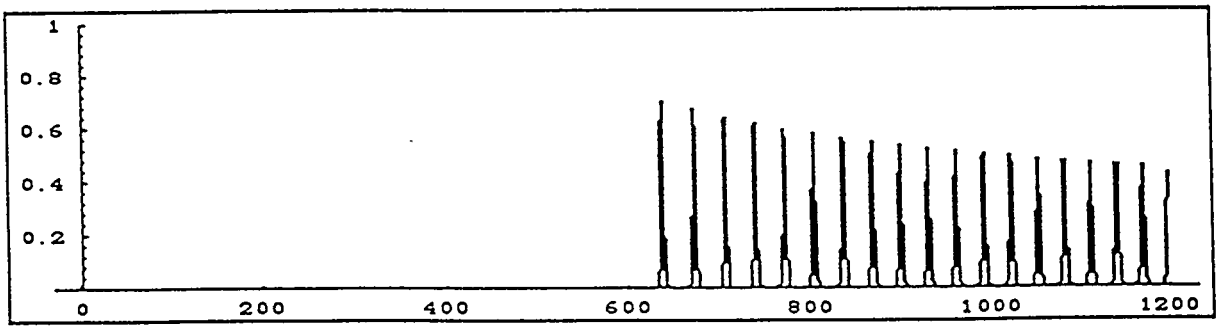

Velocity shear

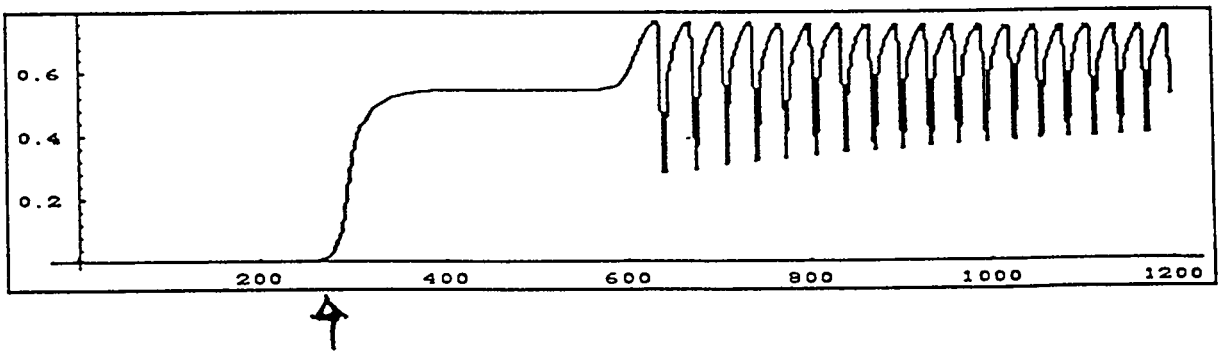

$\tilde{C} = 0$ model

Fig. 6

Input power

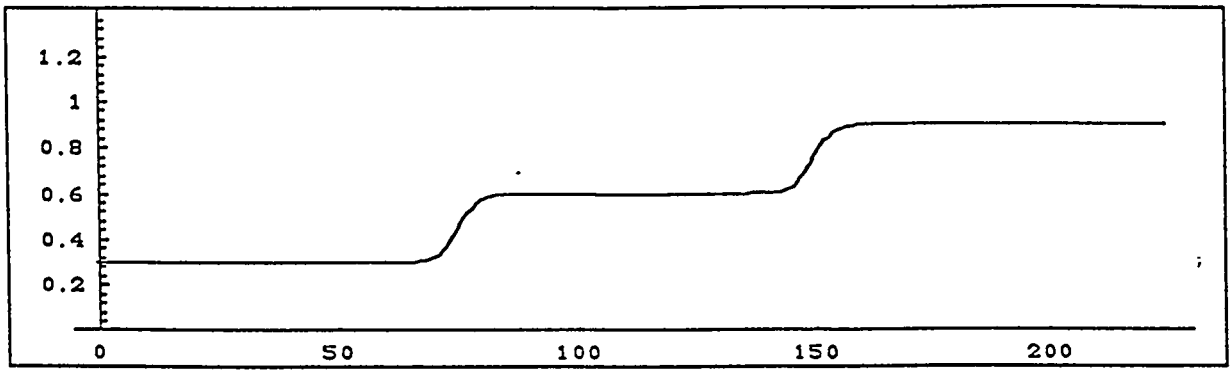

MHD fluctuations

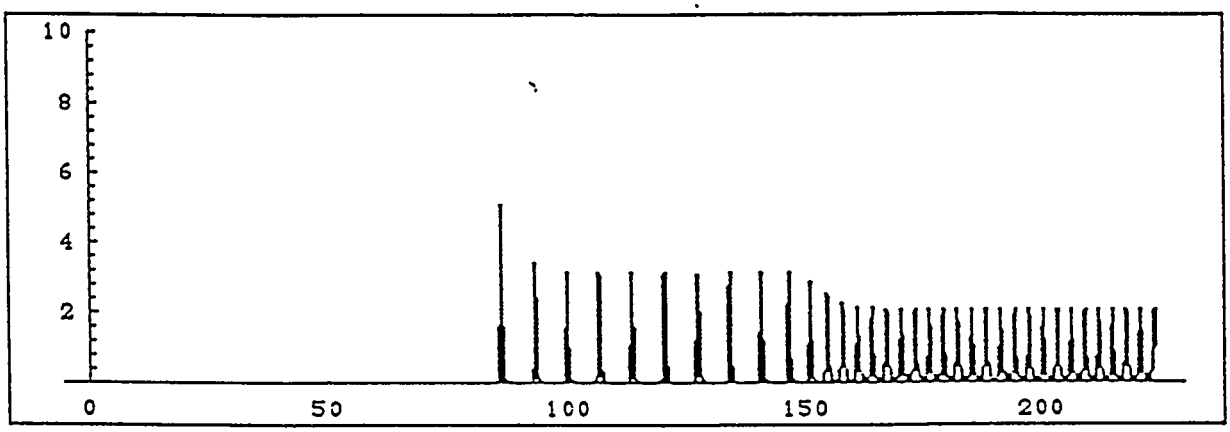

Pressure gradient

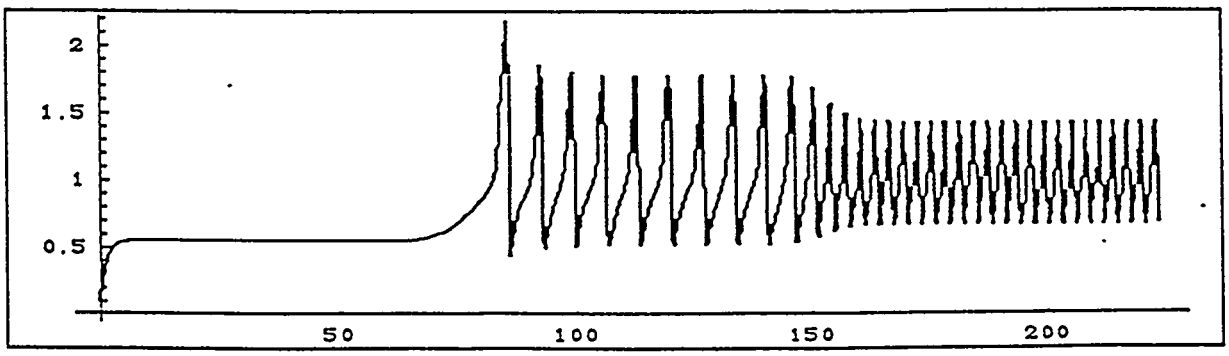

$\tilde{\mu} \to \infty$ model

Fig. 7

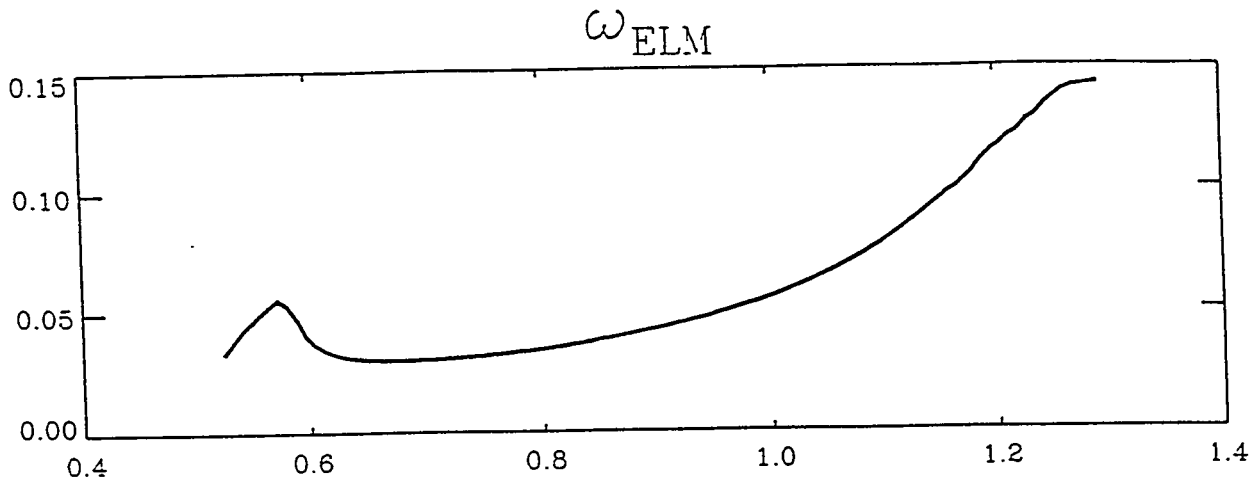

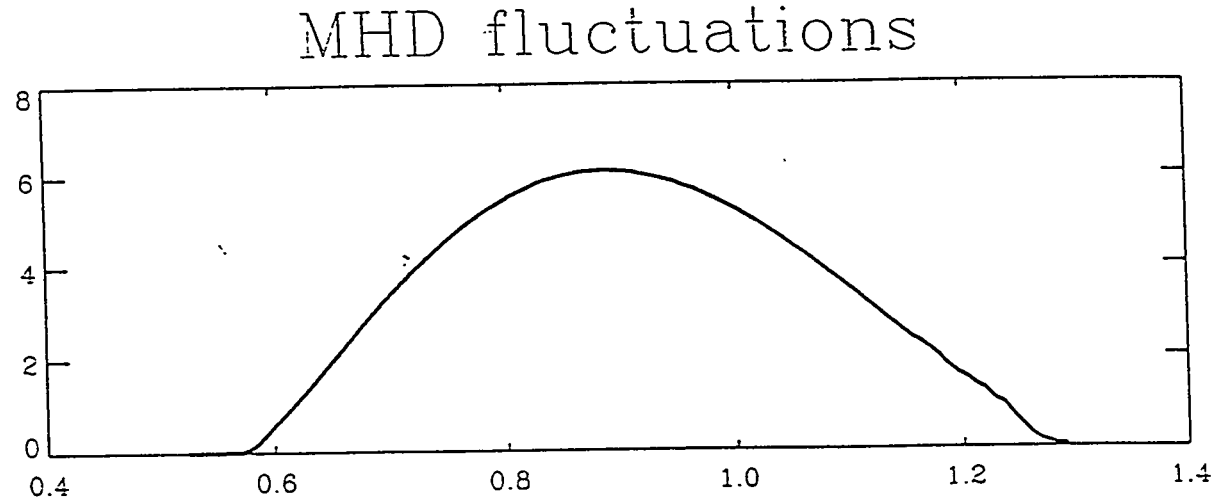

$\alpha \to 0$

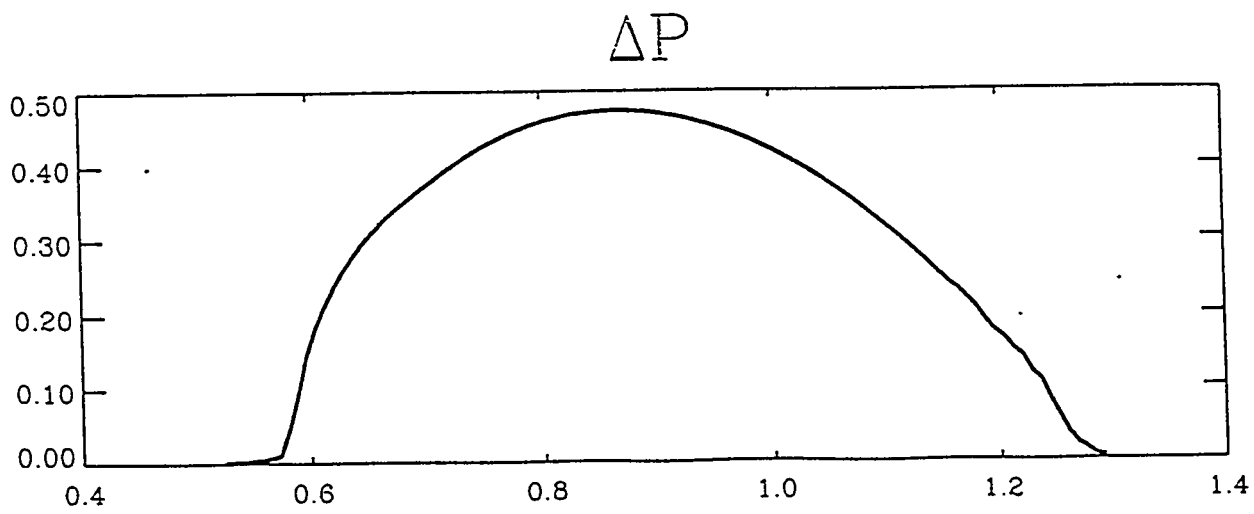

Fig. 8

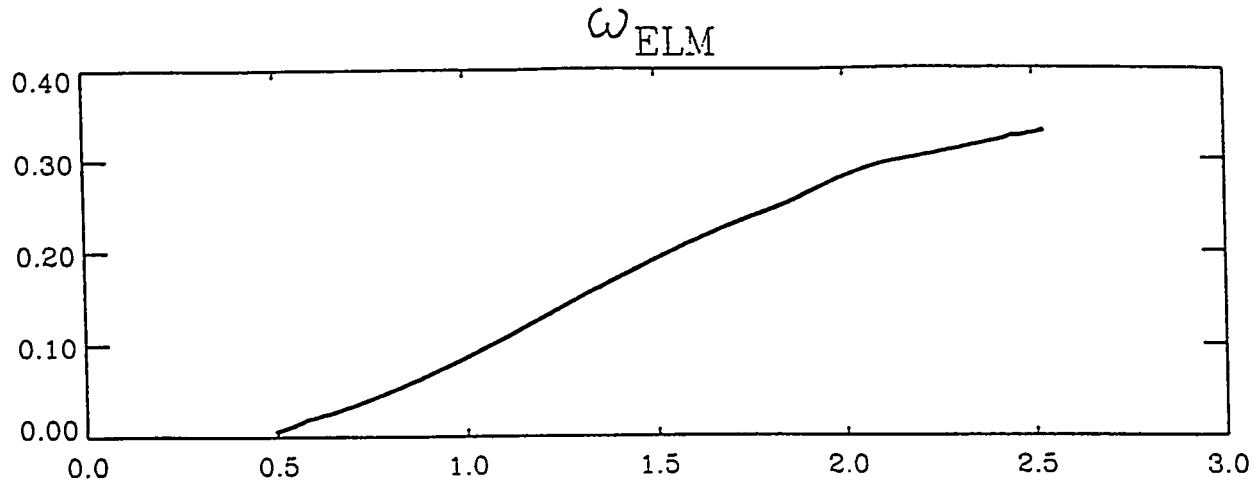

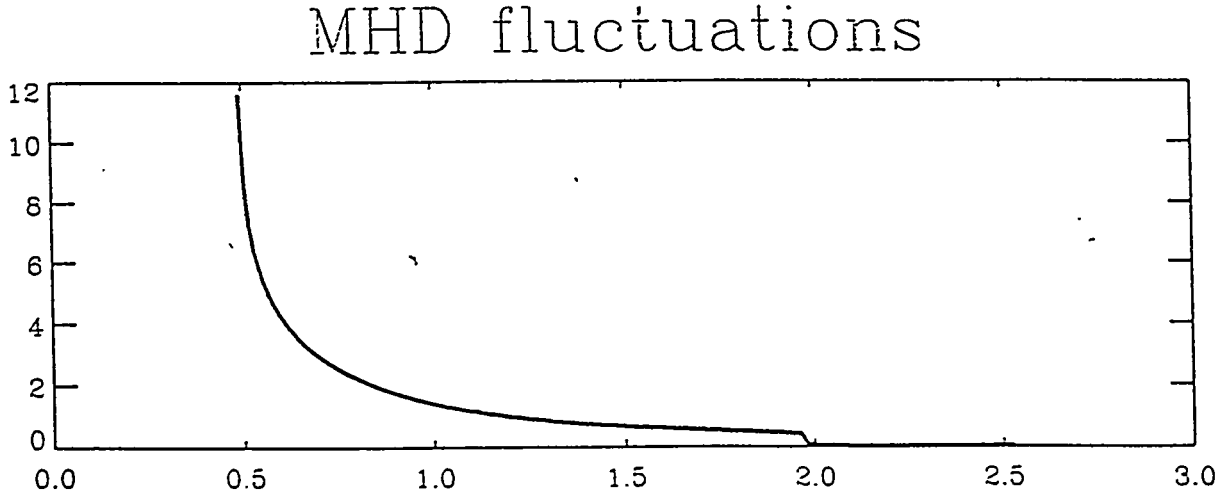

$\tilde{u} \to \infty$

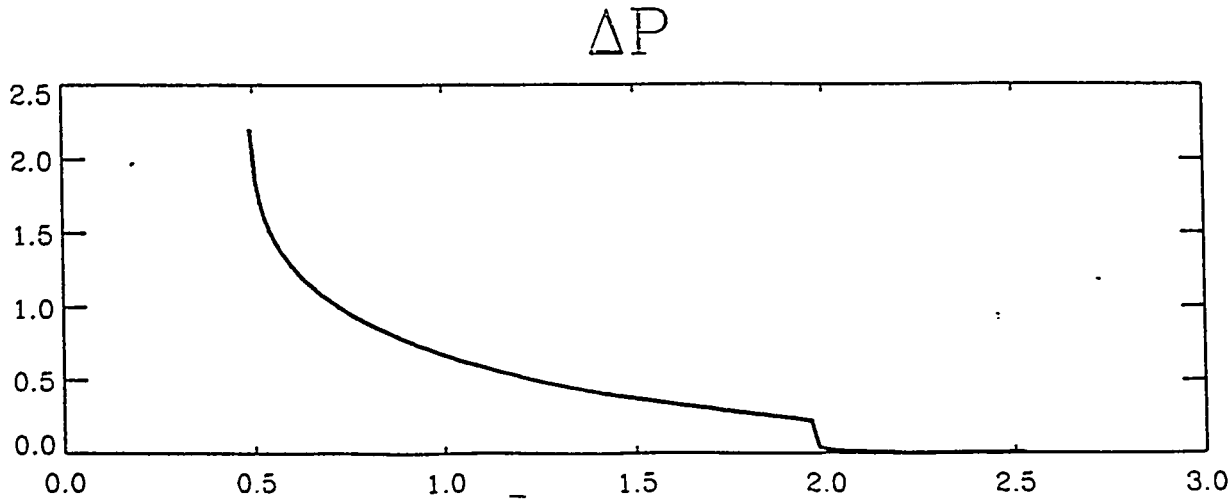

Fig. 9

Input power

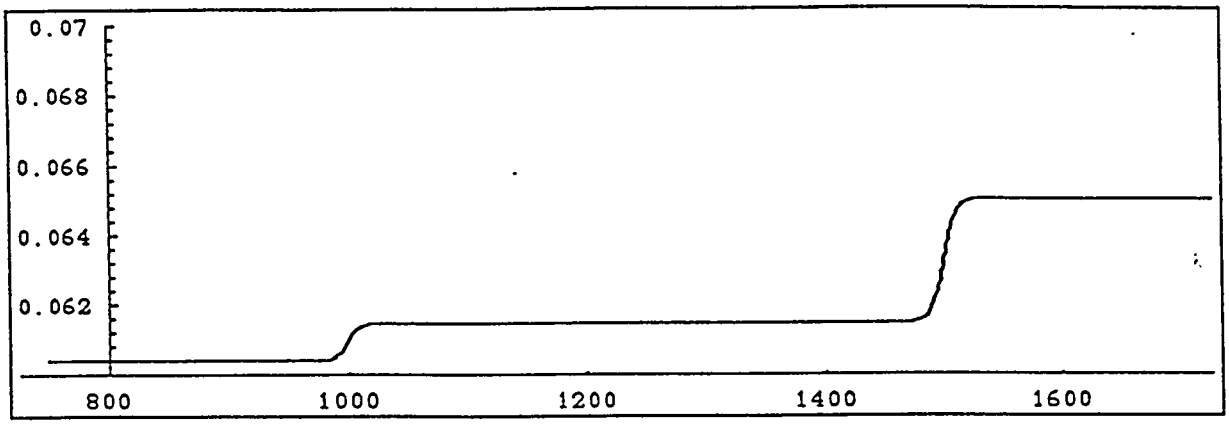

MHD fluctuations

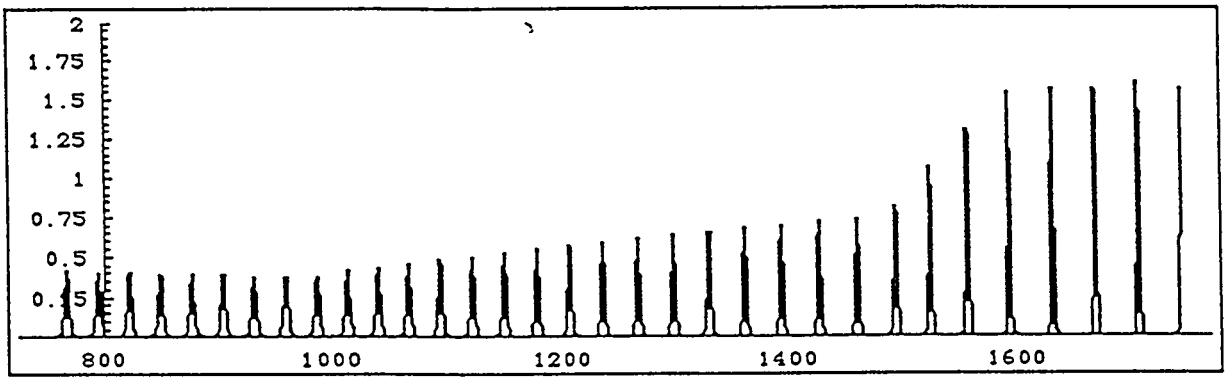

Pressure gradient

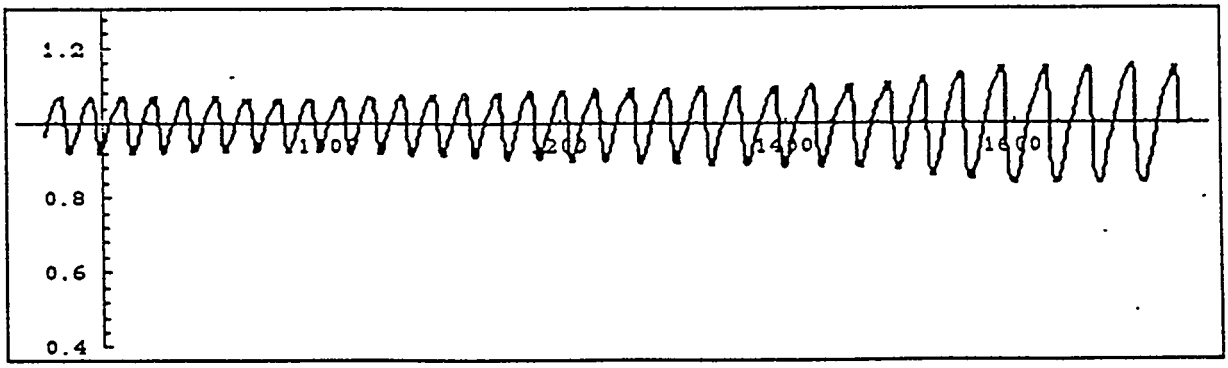

$\tilde{c} = 0$

Fig. 10

Input power

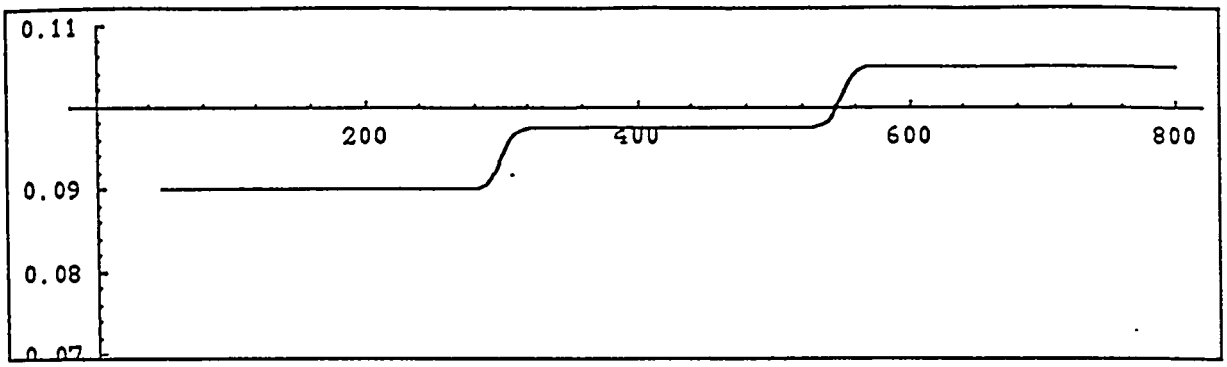

MHD fluctuations

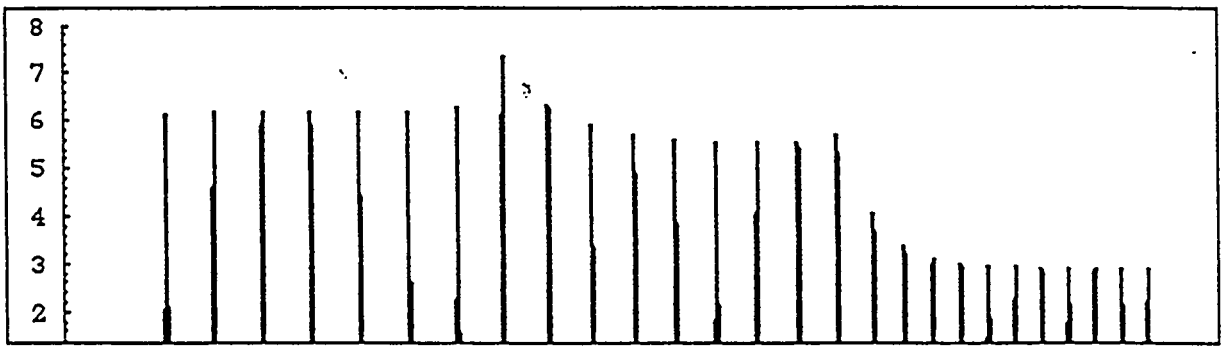

Pressure gradient

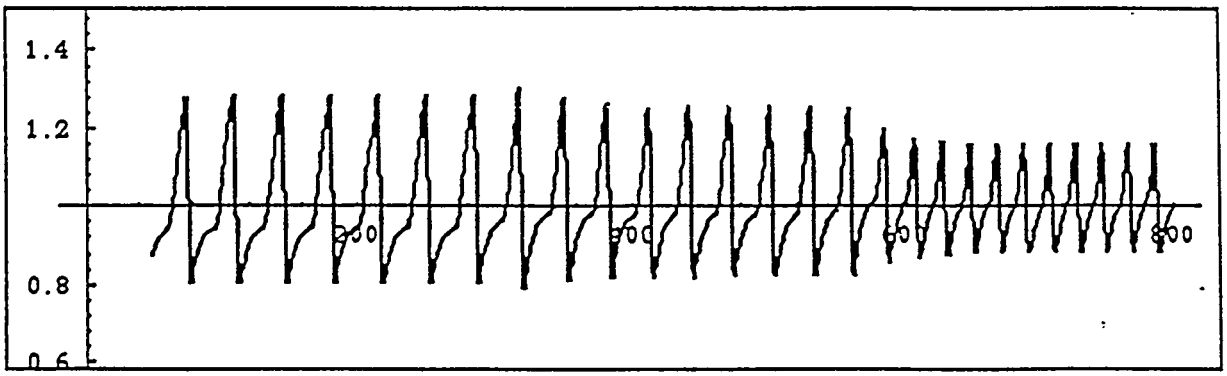

$\tilde{C} = 0$

Fig. 11

Input power

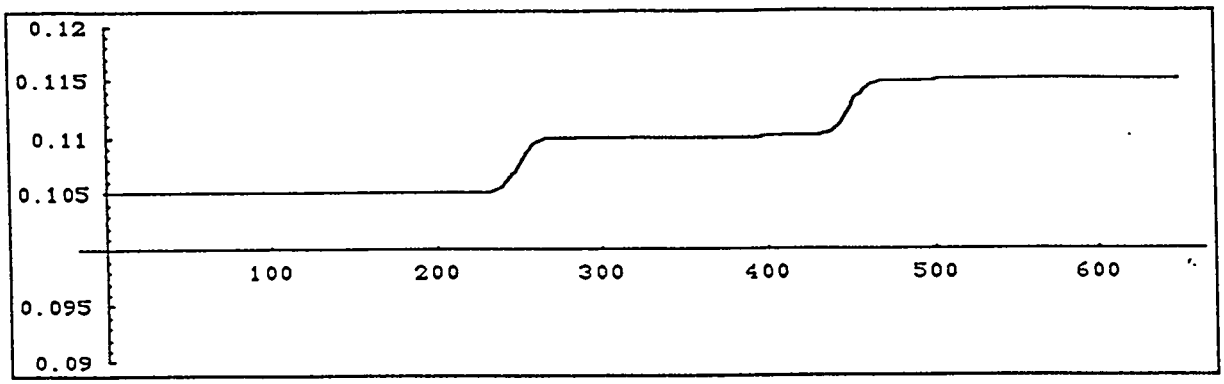

MHD fluctuations

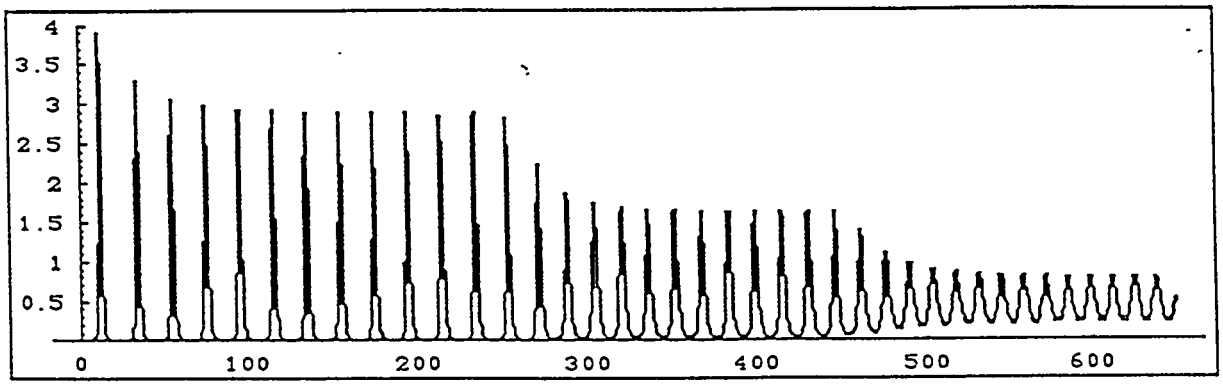

Pressure gradient

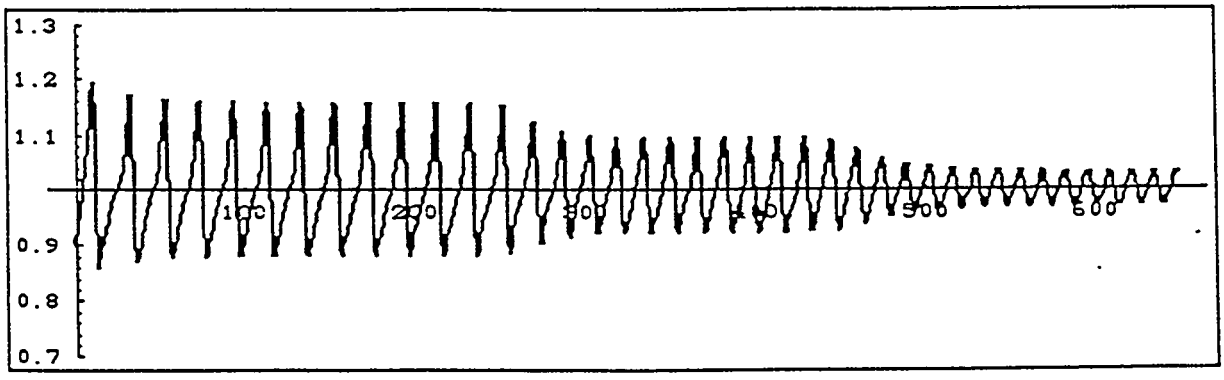

$\tilde{c} = 0$

Fig. 12

Input power

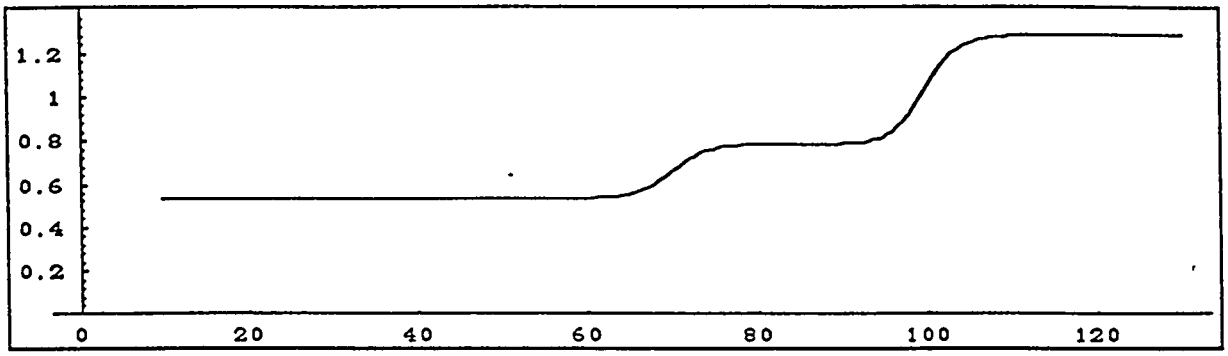

MHD- fluctuations

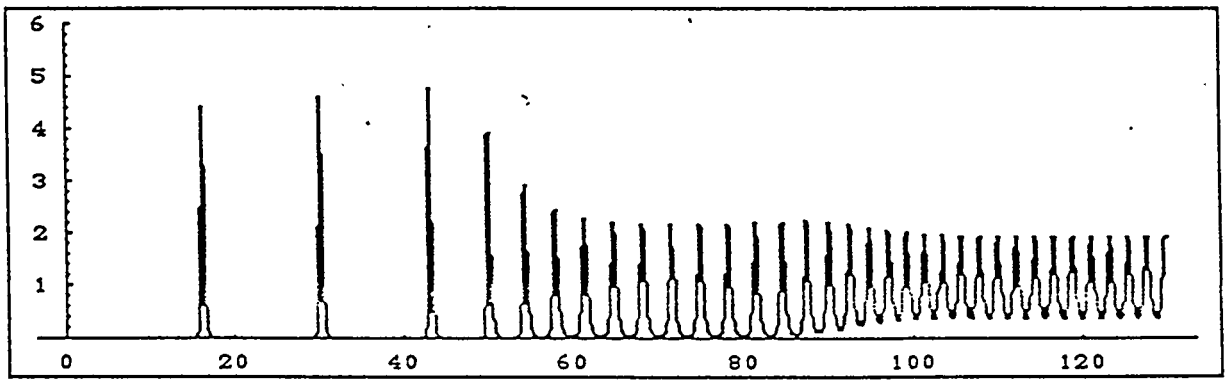

Pressure gradient

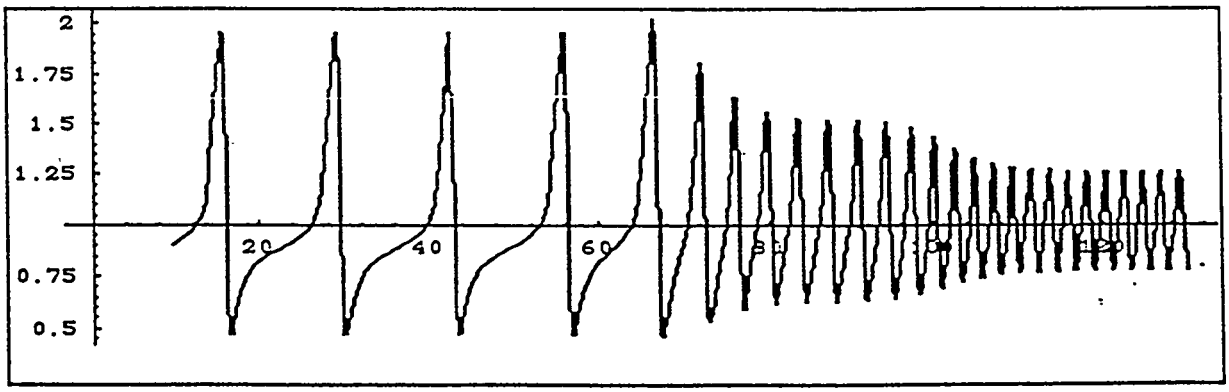

$\tilde{u} \to \infty$

Fig. 13

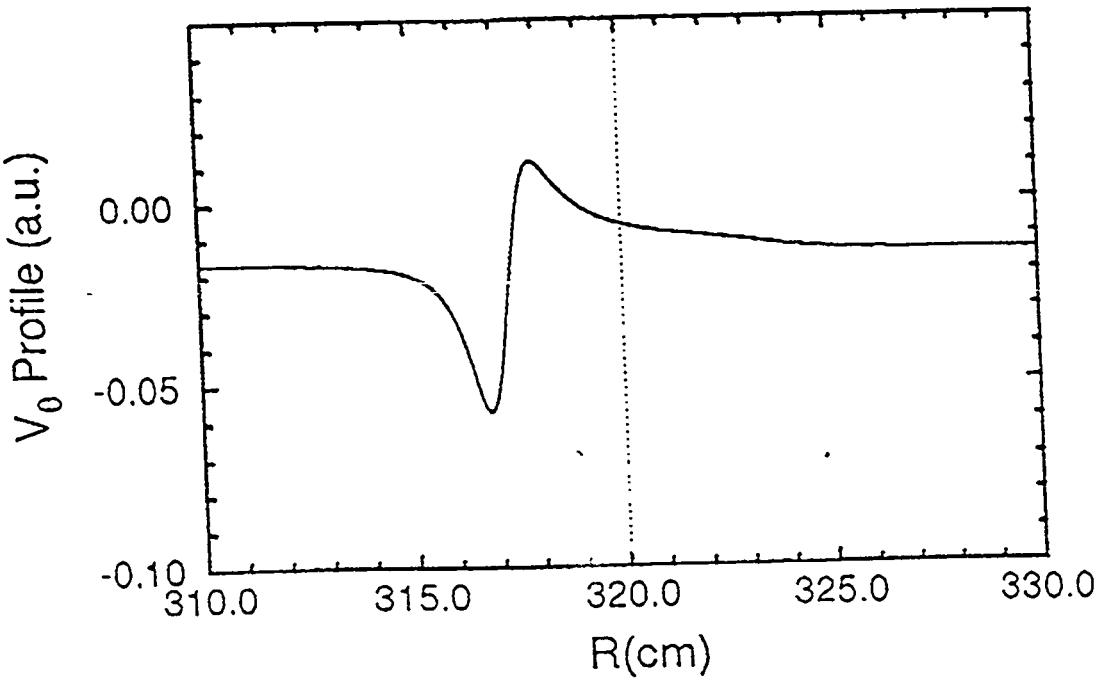

Fig. 14

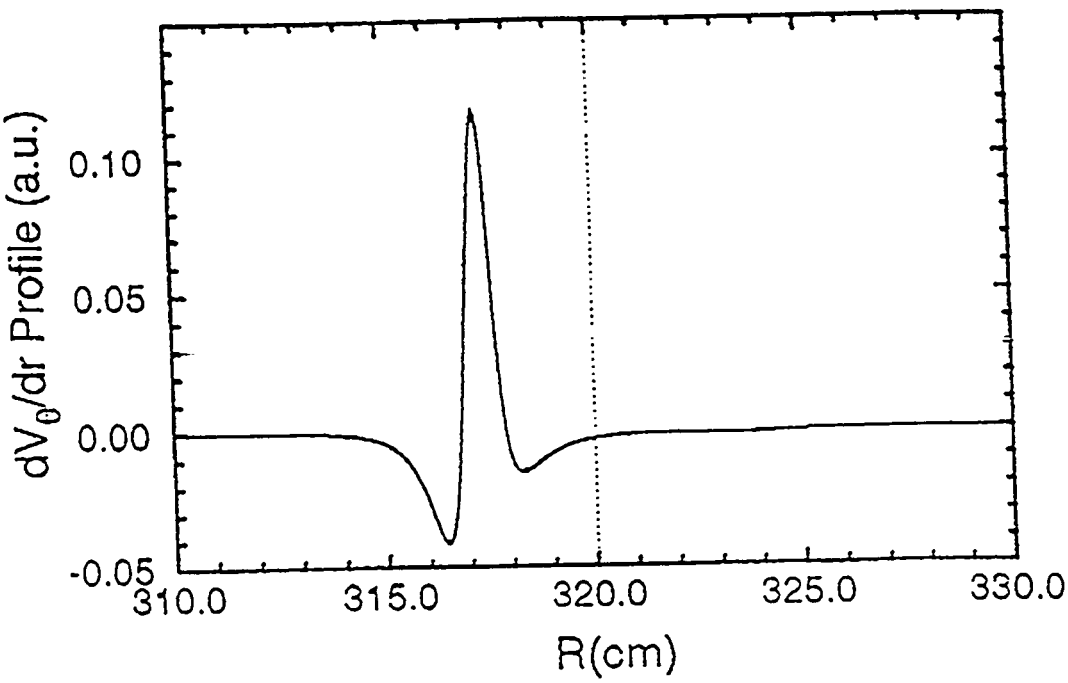

Fig. 15

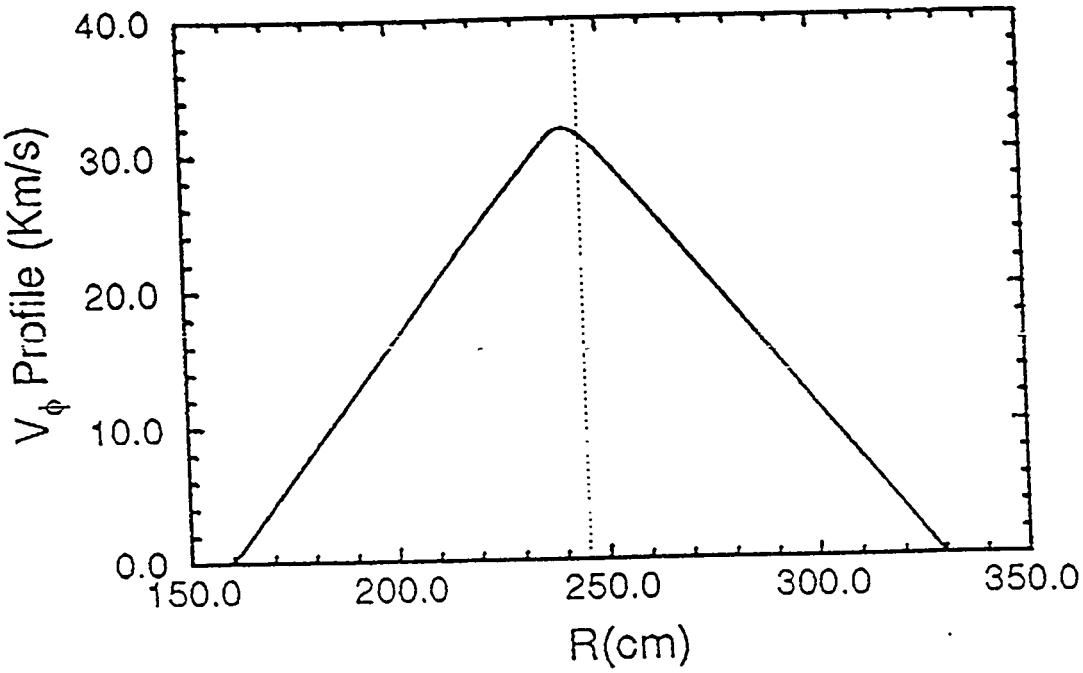
40.0
30.0
20.0
10.0
0.0
V_ϕ Profile (Km/s)
150.0
200.0
250.0
300.0
350.0
R(cm)

Fig. 16